A&A 620, A82 (2018)
https://doi.org/10.1051/0004-6361/201833520

Astronomy & Astrophysics

SUPER

I. Toward an unbiased study of ionized outflows in z ∼ 2 active galactic nuclei: survey overview and sample characterization⋆

C. Circosta[1,2], V. Mainieri[1], P. Padovani[1], G. Lanzuisi[3,4], M. Salvato[5,6], C. M. Harrison[1], D. Kakkad[1,2,7], A. Puglisi[8,9], G. Vietri[6,1], G. Zamorani[4], C. Cicone[10], B. Husemann[11], C. Vignali[3,4], B. Balmaverde[10], M. Bischetti[12,13], A. Bongiorno[12], M. Brusa[3,4], S. Carniani[14,15], F. Civano[16], A. Comastri[4], G. Cresci[17], C. Feruglio[18], F. Fiore[18], S. Fotopoulou[19], A. Karim[20], A. Lamastra[12,21], B. Magnelli[20], F. Mannucci[17], A. Marconi[22,17], A. Merloni[5], H. Netzer[23], M. Perna[17], E. Piconcelli[12], G. Rodighiero[24], E. Schinnerer[11], M. Schramm[25], A. Schulze[25], J. Silverman[26], and L. Zappacosta[12]

(Affiliations can be found after the references)

Received 28 May 2018 / Accepted 3 September 2018

ABSTRACT

Theoretical models of galaxy formation suggest that the presence of an active galactic nucleus (AGN) is required to regulate the growth of its host galaxy through feedback mechanisms, produced by, for example, AGN-driven outflows. Although many observational studies have revealed that such outflows are common both at low and high redshift, a comprehensive picture is still missing. In particular, the peak epoch of galaxy assembly ($1 < z < 3$) has been poorly explored so far, and current observations in this redshift range are mostly limited to targets with high chances to be in an outflowing phase. This paper introduces SUPER (a SINFONI Survey for Unveiling the Physics and Effect of Radiative feedback), an ongoing ESO's VLT/SINFONI Large Programme. SUPER will perform the first systematic investigation of ionized outflows in a sizeable and blindly-selected sample of 39 X-ray AGN at $z \sim 2$, which reaches high spatial resolutions (∼2 kpc) thanks to the adaptive optics-assisted IFS observations. The outflow morphology and star formation in the host galaxy will be mapped through the broad component of [O III]λ5007 and the narrow component of Hα emission lines. The main aim of our survey is to infer the impact of outflows on the on-going star formation and to link the outflow properties to a number of AGN and host galaxy properties. We describe here the survey characteristics and goals, as well as the selection of the target sample. Moreover, we present a full characterization of its multi-wavelength properties: we measure, via spectral energy distribution fitting of UV-to-FIR photometry, stellar masses (4×10^9–$2 \times 10^{11}\,M_\odot$), star formation rates (25–680 $M_\odot\,\mathrm{yr}^{-1}$) and AGN bolometric luminosities (2×10^{44}–$8 \times 10^{47}\,\mathrm{erg\,s}^{-1}$), along with obscuring column densities (up to $2 \times 10^{24}\,\mathrm{cm}^{-2}$) and luminosities in the hard 2–10 keV band (2×10^{43}–$6 \times 10^{45}\,\mathrm{erg\,s}^{-1}$) derived through X-ray spectral analysis. Finally, we classify our AGN as jetted or non-jetted according to their radio and FIR emission.

Key words. galaxies: active – galaxies: evolution – quasars: general – surveys – ISM: jets and outflows

1. Introduction

Supermassive black holes (SMBHs) at the center of galaxies undergo periods of gas accretion becoming visible as active galactic nuclei (AGN). The enormous amount of energy released during these growth episodes is thought to shape the evolutionary path of AGN host galaxies. It may play a significant role in regulating and even quenching star formation in the galaxy by expelling gas out of the galaxy itself or preventing gas cooling. The process by which the energy is injected by the AGN and coupled to the surrounding medium is the so-called AGN feedback (Fabian 2012; King & Pounds 2015; Harrison 2017). It can be particularly crucial at $z \sim 2$, since this redshift corresponds to the peak of star formation and SMBH accretion in the Universe (e.g., Madau & Dickinson 2014) and therefore the energy injected by the central engine into the host galaxy may be maximized. However, the full details of the specific effects this may have on the host galaxy's life are still not clear.

Feedback of AGN is invoked from a theoretical perspective (e.g., Ciotti & Ostriker 1997; Silk & Rees 1998; Di Matteo et al. 2005; King 2005; Somerville et al. 2008) to explain key observations of the galaxy population, such as the tight correlation between black hole masses and bulge masses as well as velocity dispersions of the host galaxies (Kormendy & Ho 2013), the bimodal color distribution of galaxies (Strateva et al. 2001), and the lack of very massive galaxies in the most massive galaxy haloes (Somerville et al. 2008; Behroozi et al. 2013). According to some models (e.g., King 2005; Springel et al. 2005; Debuhr et al. 2012; Costa et al. 2014), fast winds are launched by the accretion disk surrounding the SMBH and driven by radiative and mechanical energy during its active and bright phase. These winds propagate into the host galaxy coupling to the interstellar medium (ISM) and drive fast outflows out to large scales (up to ∼1000 km s^{-1} on kpc scales), potentially removing the gas which fuels star formation. It is important to test the models with observations by measuring key outflow properties such as kinetic energy and momentum injection rates (Fiore et al. 2017; Harrison et al. 2018).

AGN-driven outflows can therefore be a manifestation of AGN feedback. The presence of outflows in AGN host galaxies is now quite well established: they have been detected at different

⋆ Full Table B.1 is only available in electronic form at the CDS via anonymous ftp to cdsarc.u-strasbg.fr (130.79.128.5) or via http://cdsarc.u-strasbg.fr/viz-bin/qcat?J/A+A/620/A82

physical scales (e.g., Feruglio et al. 2010; Tombesi et al. 2015; Veilleux et al. 2017) and in different gas phases (e.g., Cano-Díaz et al. 2012; Cicone et al. 2014; Rupke et al. 2017), both in the nearby (e.g., Rupke & Veilleux 2013; Perna et al. 2017) and distant Universe (e.g., Nesvadba et al. 2011; Carniani et al. 2015; Cicone et al. 2015). An important property shown by outflows is their multi-phase nature so to fully characterize them we need to trace all the gas phases, neutral and ionized, atomic and molecular (Cicone et al. 2018). The ionized phase has been studied through absorption and emission lines in rest-frame optical (e.g., Bae et al. 2017; Concas et al. 2017; Perna et al. 2017), ultraviolet (UV) (e.g., Liu et al. 2015) and X-ray (e.g., Tombesi et al. 2010). When the velocity shift of these lines with respect to the rest-frame velocity is not representative of ordered motion in the galaxy as traced by stellar kinematics, it can be considered as evidence for the presence of non-gravitational kinematic components, such as outflowing gas (Karouzos et al. 2016; Woo et al. 2016). To understand the impact of AGN outflows on the gas and star formation in the host galaxy, it is necessary to explore large galactic scales (∼1−10 kpc). A commonly used diagnostic for this kind of studies is the forbidden emission line doublet [O III]λ5007,4959 Å. It traces the kinematics of ionized gas on galaxy-wide scales, in the narrow line region (NLR), since being a forbidden line it cannot be produced in the high-density environment of the broad line region (BLR) on sub-parsec scales. Therefore asymmetric [O III]λ5007 profiles, showing a broad and blue-shifted wing, are used to trace outflowing kinematic components.

Long-slit optical and near-infrared (NIR) spectroscopy is a useful technique to reveal outflow signatures (e.g., Das et al. 2005; Crenshaw & Kraemer 2007; Brusa et al. 2015). However, it is able to provide spatial information along one direction, therefore lacking a detailed mapping of the outflow distribution in the host galaxy together with its velocity. In recent years, integral-field spectroscopy (IFS) studies have offered a more direct way to identify and interpret outflows, allowing astronomers to spatially resolve the kinematics of ionized gas (e.g., Cresci et al. 2009; Alexander et al. 2010; Gnerucci et al. 2011; Förster Schreiber et al. 2014; Harrison et al. 2014). Nevertheless, the observational evidence available so far at $z > 1$, the crucial cosmic epoch to study AGN-driven outflows and on which this paper will be focused, is sparse, mainly limited to bright objects or observations performed in seeing limited conditions and therefore not able to resolve scales below 3−4 kpc, which limits how well the observations can constrain model predictions (Harrison et al. 2018). In Fig. 1 we collect IFS results from the literature tracing ionized outflows in AGN host galaxies through the [O III] emission line. The left panel compares AGN bolometric luminosities and redshift for each target, in order to summarize the state-of-the-art of ionized AGN outflow IFS studies. Contrary to the uniform coverage of the parameter space at $z < 1$ (gray crosses in Fig, 1, left panel), at $z > 1$ it is limited to a small number of objects, mainly at high luminosity ($L_{\rm bol} > 10^{46}$ erg s^{-1}, see points in Fig. 1, left panel). The targets of previous studies are mostly selected to increase the chances to detect an outflow, meaning because they are powerful AGN (e.g., in the IR or radio regime), they have already known outflows or characteristics suitable for being in an outflowing phase (e.g., high mass accretion rate of the SMBH and high column density; Brusa et al. 2015; Kakkad et al. 2016). Because of this observational bias, it is still controversial how common these outflows are especially in sources with low AGN bolometric luminosity. Nevertheless, detailed single object studies have provided evidence that powerful outflows may suppress star formation in the regions where they are detected (e.g., Cano-Díaz et al. 2012; Cresci et al. 2015; Carniani et al. 2016), although it is still not clear the impact that such outflows may have on the global star-forming activity occurring in the host galaxy (i.e., including regions of the galaxies not affected by the outflow). In addition to negative feedback mechanisms, outflows have been proved to be responsible for positive feedback mechanisms in a few cases by triggering star formation (e.g., Cresci et al. 2015; Molnár et al. 2017; Cresci & Maiolino 2018).

In order to draw a coherent picture and definitively address the impact of such outflows on the galaxy population evolution it is necessary to conduct systematic and unbiased searches for outflows in large samples of objects. The KMOS AGN Survey at High redshift (KASHz; Harrison et al. 2016; Harrison et al., in prep.; blue rectangle in Fig. 1, left panel) has first started to provide spatially-resolved information for hundreds of X-ray selected AGN. These observations are seeing limited, which sets a limit on the spatial scales that can be resolved at $z > 1$. The range of spatial scales resolved in current observations is shown in the right panel of Fig. 1, plotted as a function of redshift for the same collection of data as in the left panel. At $z > 1$, the spatial resolution is mainly in the range 3−10 kpc (i.e. >0.5″).

To provide higher spatial resolutions (down to ∼2 kpc at $z \sim 2$), one needs to exploit the possibilities offered by adaptive optics (AO), which corrects for the distortion caused by the turbulence of the Earth's atmosphere. This has been done by, for example, Perna et al. (2015), Brusa et al. (2016), Vayner et al. (2017) and Vietri et al. (2018). Such observations require a larger amount of observing time, therefore it is necessary to focus on smaller but still representative samples. Our on-going ESO Large Programme called SUPER (the SINFONI Survey for Unveiling the Physics and Effect of Radiative feedback), represented by the red rectangle in Fig. 1, is taking advantage of the AO corrections by reaching angular resolutions of 0.2″. It combines spatially-resolved AO-assisted IFS observations for a fairly representative sample of sources selected in an unbiased way with respect to the chance of detecting outflows. This survey aims at investigating the physical properties of AGN outflows and their impact on the star formation activity in the host galaxies as well as connecting the physical properties of AGN and host galaxies to those of ionized outflows. As shown in Fig. 1, SUPER probes a wide range of AGN bolometric luminosities, up to four orders of magnitude, with spatial resolutions between ∼1.7 and 4 kpc (i.e., 0.2″−0.5″).

This paper is the first of a series of publications dedicated to the survey. It focuses on providing an overview of the survey (i.e., characteristics, goals and sample selection criteria), as well as describing the physical properties of the target sample and the way they have been measured through a uniform multi-wavelength analysis from the X-ray to the radio regime. We derive stellar masses, star formation rates (SFRs) and AGN bolometric luminosities from the multi-wavelength spectral energy distributions (SEDs), X-ray luminosities and column densities from the X-ray spectra and BH masses and Eddington ratios from the optical spectra. The paper is organized as follows: in Sect. 2 we present the properties and the main goals of the survey as well as the sample selection criteria and its X-ray properties. In Sect. 3 we describe the multi-wavelength dataset and the SED-fitting code used to derive host galaxy and AGN properties of the targets. These properties are then discussed in Sect. 4, with particular emphasis on stellar masses, SFRs and AGN bolometric luminosities as well as the target properties in the radio regime. We finally summarize our results and discuss future follow-up work in Sect. 5. In this paper we adopt a *WMAP9* cosmology (Hinshaw et al. 2013), $H_0 = 69.3$ km s^{-1} Mpc^{-1}, $\Omega_{\rm M} = 0.287$ and $\Omega_\Lambda = 0.713$.

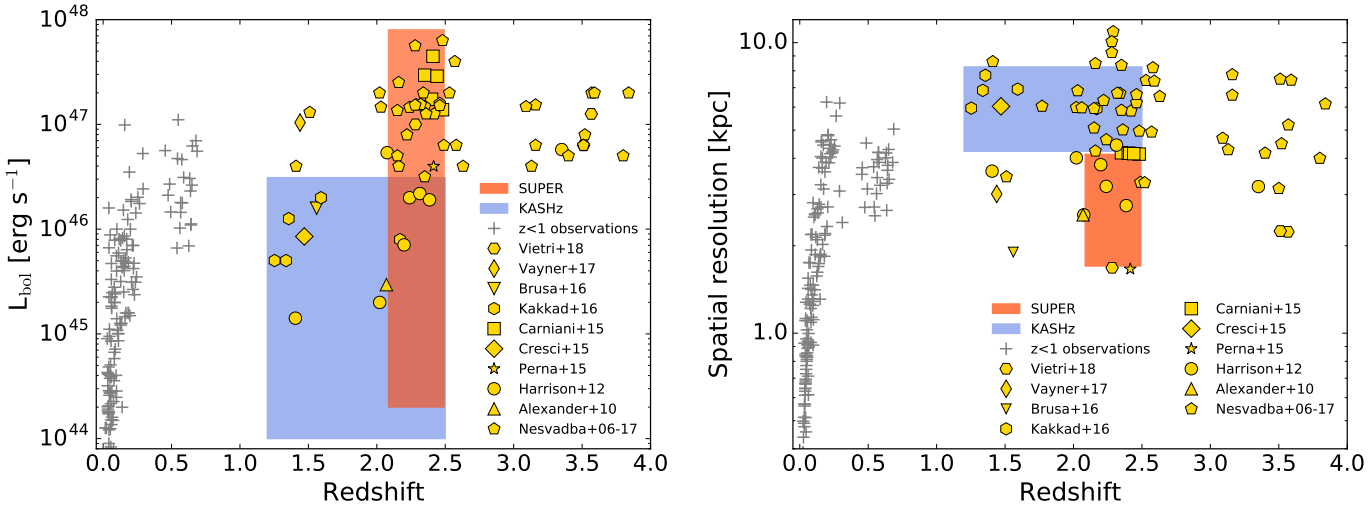

Fig. 1. Summary of IFS observations from the literature characterizing ionized outflows through the [O III]λ5007 emission line in AGN host galaxies. *Left panel*: for each observation we plot the AGN bolometric luminosity of the source, in units of erg s^{-1}, as a function of redshift. The red and blue shaded areas show the parameter space probed by SUPER and KASHz (Harrison et al. 2016; Harrison et al., in prep.), respectively. Excluding these two surveys, current observations at $z > 1$ are limited to a smaller number of objects, mainly at high luminosity ($L_{bol} > 10^{46}$ erg s^{-1}) and focused on targets mostly selected to increase the chances to detect an outflow. SUPER will be able to explore a wide range in bolometric luminosities ($10^{44} < L_{bol} < 10^{48}$ erg s^{-1}) for an unbiased sample of AGN. The gray crosses represent observations at $z < 1$ (Bae et al. 2017; Rupke et al. 2017; Karouzos et al. 2016; Harrison et al. 2014; Husemann et al. 2013, 2014, 2017b; Liu et al. 2013, 2014) covering the parameter space much more uniformly than high-redshift observations available so far (Vietri et al. 2018; Vayner et al. 2017; Brusa et al. 2016; Kakkad et al. 2016; Carniani et al. 2015; Cresci et al. 2015; Perna et al. 2015; Harrison et al. 2012; Alexander et al. 2010; Nesvadba et al. 2006, 2007, 2008, 2011, 2017a,b). All AGN bolometric luminosities, when not available in the papers, have been obtained consistently either as indicated in the papers themselves or from the observed [O III] luminosity adopting a conversion factor of 3500 (Heckman et al. 2004). *Right panel*: Spatial resolution, in kpc, of the observations shown in the left panel as a function of redshift. The angular resolutions from which the values plotted are derived, are taken from the respective papers and given by the seeing of the observations or from the size of the PSF. SUPER observations will allow us to reach an unprecedented spatial resolution (i.e. ~1.7−4 kpc) for a sizeable sample of 39 AGN, obtained just by a few single-object studies so far at similar redshift.

2. The survey

SUPER[1] (PI: Mainieri – 196.A-0377) is a Large Programme at the ESO's Very Large Telescope (VLT). The survey has been allocated 280 h of observing time in AO-assisted mode with the aim of providing high-resolution, spatially-resolved IFS observations of multiple emission lines for a carefully-selected sample of 39 X-ray AGN at $z \sim 2$. The AO correction is performed in Laser Guide Star-Seeing Enhancer (LGS-SE) mode, which has demonstrated the capability to achieve a point spread function (PSF) full width at half maximum (FWHM) of ~0.3″ under typical weather conditions in Paranal (Förster Schreiber et al. 2018), i.e., average seeing of ~0.55″ in K band (Sarazin et al. 2008). We have selected for all our targets the 50 mas pixel^{-1} scale of SINFONI which corresponds to a total field of view FOV = 3.2″ × 3.2″. The selected plate scale corresponds to a spectral resolution of about $R \approx 2730$ in H band and $R \approx 5090$ in K band.

The redshift range covered by SUPER is crucial to investigate AGN feedback, being at the peak epoch of AGN and galaxy assembly. Key emission lines, such as [O III], Hβ and Hα, are covered with H- and K-band observations in this redshift range. We will use asymmetric and spatially-extended [O III] line emission, traced by H-band observations, to identify outflowing ionized gas as extensively done in the literature (e.g., Alexander et al. 2010; Cresci et al. 2015; Harrison et al. 2016). The K-band observations will provide the possibility to map the Hα emission, with the aim to construct spatially-resolved maps of the on-going star formation in the host from the narrow component of the line, which could be less affected by AGN emission, and compare it with the outflow geometry derived from the [O III] line profile (see, e.g., Cano-Díaz et al. 2012; Cresci et al. 2015; Carniani et al. 2016). The comparison between these two tracers will give us the opportunity to constrain systematically the role of AGN outflows in regulating star formation. Thanks to the extensive set of AGN and host galaxy physical properties (AGN bolometric luminosity, BH mass, Eddington ratio, obscuring column density, radio emission, stellar mass and SFR), derived in a uniform way for each target as explained in the present paper, and outflow parameters which will be extracted from the H-band observations (such as mass outflow rate, kinetic power, momentum rate, size), SUPER will explore the potential relations among these quantities (Fiore et al. 2017).

The science goals of our survey are:

- Systematic study of the occurrence of outflows in AGN host galaxies and investigation of any possible link between the physical properties of both SMBHs and their hosts, and the outflow properties.
- Mapping AGN ionized outflow morphology on kpc scale using [O III] and constraining their impact on the on-going star formation in the host galaxies using the narrow component of Hα. If the signal-to-noise of the latter is not good enough to produce spatially-resolved maps of star formation, we should still be able to compare the outflow properties with the integrated SFR (as derived by SED fitting).
- Investigating the variation of outflow properties as a function of the host galaxy location with respect to the main sequence of star-forming galaxies (MS, e.g., Noeske et al. 2007), in order to investigate empirically the relation between galaxy and AGN.

An important further goal of this survey will be the comparison of our results to a mass-matched control sample of normal

[1] http://www.super-survey.org

star-forming galaxies at the same redshift and with similar AO-assisted observations (e.g., the SINS/zC-SINF survey, Förster Schreiber et al. 2018, see Sect. 4.1.5), to investigate the differences between galaxies hosting active and inactive SMBHs.

In the following we describe the criteria adopted to select our sample.

2.1. Sample selection

Our Large Programme is designed to conduct a blind search for AGN-driven outflows on a representative sample of AGN. Therefore, we do not preselect AGN with already known outflows or with characteristics suitable for being in an outflowing phase (Brusa et al. 2015; Kakkad et al. 2016). Instead, aiming at performing a statistical investigation of this phenomenon, the first goal is to cover the widest possible range in AGN properties.

One of the most efficient tracers of AGN activity is offered by their X-ray emission, since it probes directly the active nucleus with a negligible contamination from the host galaxy, providing the largest AGN surface density (e.g., Padovani et al. 2017). We identified our targets by combining X-ray catalogs from several surveys characterized by different depths and areas. While shallow and wide-field surveys provide a better census of the rare high-luminosity AGN, deep and small-area surveys, limited to a few deg^2, are able to reveal fainter sources (see Fig. 3 in Brandt & Alexander 2015). By adopting this "wedding cake" approach we are able to cover a wide range in AGN bolometric luminosity, $10^{44} < L_{\rm bol} < 10^{48}$ erg s^{-1} (see Fig. 1), spanning both faint and bright AGN. The selection was performed by adopting as a threshold an absorption-corrected X-ray luminosity $L_{\rm X} \geq 10^{42}$ erg s^{-1} from the following surveys:

- The *Chandra* Deep Field-South (CDF-S; Luo et al. 2017), the deepest X-ray survey to date which covers a global area of 484.2 arcmin^2 observed for a total *Chandra* exposure time of ∼7 Ms, reaching a sensitivity of $\sim 1.9 \times 10^{-17}$ erg cm^{-2} s^{-1} in the full 0.5−7.0 keV band.
- The COSMOS-Legacy survey (Civano et al. 2016; Marchesi et al. 2016a), a 4.6 Ms *Chandra* observation of the COSMOS field, which offers a unique combination of deep exposure over an area of about 2.2 deg^2 at a limiting depth of 8.9×10^{-16} erg cm^{-2} s^{-1} in the 0.5−10 keV band.
- The wide-area *XMM-Newton* XXL survey (Pierre et al. 2016), where we focus in particular on the equatorial subregion of the XMM-XXL North, a ∼25 deg^2 field surveyed for about 3 Ms by *XMM-Newton* with a sensitivity in the full 0.5−10 keV band of 2×10^{-15} erg cm^{-2} s^{-1}.
- The Stripe 82 X-ray survey (Stripe82X; LaMassa et al. 2016; Ananna et al. 2017), ∼980 ks of observing time with *XMM-Newton* covering 31.3 deg^2 of the Sloan Digital Sky Survey (SDSS) Stripe 82 Legacy Field and a flux limit of 2.1×10^{-15} erg cm^{-2} s^{-1} in the full 0.5−10 keV band.
- The WISE/SDSS selected Hyper-luminous quasars sample (WISSH; Bischetti et al. 2017; Duras et al. 2017; Martocchia et al. 2017; Vietri et al. 2018), with both proprietary and archival *Chandra* and *XMM-Newton* observations available, described in Martocchia et al. (2017).

The choice of the fields was driven by their visibility from Paranal and the rich multi-wavelength photometric coverage from the UV to the far-infrared (FIR), needed to obtain robust measurements of the target properties by using an SED-fitting technique. Our targets are then selected to meet the following criteria:

1. Spectroscopic redshift in the range $z = 2.0-2.5$, whose quality was flagged as "Secure" in the respective catalogs. This redshift range was chosen in order to have Hβ and [O III] included in H-band and Hα in K-band together with their potential broad line components, by allowing a margin of 10 000 km s^{-1} between the peak of the lines and the edges of the filter bands.
2. Observed wavelengths for [O III] and Hα characterized by a low contamination from the strong telluric OH lines, which affect NIR observations.

The resulting sample consists of 39 AGN (namely 6 from CDF-S, 16 from COSMOS, 10 from XMM-XXL, 4 from Stripe82X and 3 from the WISSH sample), whose IDs, coordinates, redshifts as well as $H-$ and $K-$band magnitudes (AB) are reported in Table A.1. This sample results from an optimization between size, the amount of observing time required to carry out the observations, and a wide and uniform coverage in AGN bolometric luminosities, Eddington ratios, and column densities. All our targets have spectroscopic redshifts based on optical spectroscopic campaigns: for example VLT/VIMOS and FORS2 surveys for the CDF-S (Balestra et al. 2010; Kurk et al. 2013); for the COSMOS field, a master spectroscopic catalog is available within the COSMOS collaboration (Salvato et al., in prep.) and includes results from several spectroscopic surveys of this field (see Marchesi et al. 2016a); SDSS-BOSS spectra for the XMM-XXL field (Menzel et al. 2016); SDSS-DR12 for Stripe82X (LaMassa et al. 2016); SDSS-DR10 and LBT/LUCI1 redshifts for the WISSH subsample (Bischetti et al. 2017). Thanks to the parameter space covered by the survey (Fig. 1, left panel), we will be able to probe AGN bolometric luminosities in the range $44 \lesssim \log(L_{\rm bol}/{\rm erg\,s^{-1}}) \lesssim 48$, not covered so far by a coherent high spatial resolution observing program at this redshift.

2.2. X-ray properties of the sample

As described in Sect. 2.1, our survey sample is selected from available X-ray AGN surveys. Apart from the source detection, these X-ray observations provide us with important information on the AGN properties from the analysis of their X-ray spectra. Since the obscuring column densities $N_{\rm H}$ and the X-ray luminosities $L_{\rm X}$ available from the various survey catalogs may be affected by inhomogeneities due to the adoption of different analysis methods and spectral models, we decided to perform a new systematic analysis of all the X-ray spectra, by using XSPEC v.12.9.1[2] (Arnaud 1996). For this purpose, we followed the method described in Lanzuisi et al. (2013) and Marchesi et al. (2016b) for *XMM-Newton* and *Chandra* data respectively, which have been extensively tested in the low count regime typical of the current data set. *Chandra* and *XMM-Newton* spectra of sources in the COSMOS field are extracted following Lanzuisi et al. (2013) and Mainieri et al. (2011), respectively. For sources in the CDF-S we followed the approach described in Vito et al. (2013), applied to the full 7 Ms data set (Luo et al. 2017). For sources in XMM-XXL, Stripe82X and WISSH (SDSS targets), we extracted new *XMM-Newton* spectra adopting a standard data reduction procedure[3] (background flare removal, "single" and "double" event selection, CCD edge and bad pixels removal) and standard source, background and response matrix extraction from circular regions, whose radii were chosen to maximize the signal-to-noise ratio (e.g., Liu et al. 2016, for XMM-XXL). Typical background regions are ∼10 times the source extraction regions. We considered the 0.5−7.0 keV band for *Chandra* and 0.5−10 keV band for *XMM-Newton*. All the fits were performed

[2] https://heasarc.gsfc.nasa.gov/xanadu/xspec/

[3] We used SAS v.16.0.0, https://heasarc.gsfc.nasa.gov/docs/xmm/xmmhp_analysis.html

by using the Cash statistic (Cash 1979) and the direct background option (Wachter et al. 1979). The spectra were binned to 1 count per bin to avoid empty channels.

For sources with more than 30 (50) net counts (reported in Table A.2) for *Chandra* (*XMM-Newton*), we performed a simple spectral fit, modeling the emission with an absorbed power law plus Galactic absorption as well as a secondary power law to reproduce any excess in the soft band, due to scattering or partial covering in obscured sources. In 11 cases out of 39 this second component gave a significant contribution to the fit, while in the other cases its normalization was consistent with 0. The photon index was left free to vary during the spectral analysis for spectra with more than ∼100 net counts (typical values within $\Gamma = 1.5-2.5$), otherwise we fixed it to the canonical value of 1.8 (e.g., Piconcelli et al. 2005), being mainly interested in deriving reliable $N_{\rm H}$ and $L_{\rm X}$ values. For targets with less than 30 (50) counts, we relied on hardness ratios ($\rm HR = \frac{H-S}{H+S}$, where H and S are the number of counts in the hard 2−7 keV and soft 0.5−2 keV bands, respectively), converted into $N_{\rm H}$ values at the source redshift following Lanzuisi et al. (2009).

Both in the case of spectral analysis and HR, we propagated the uncertainty on $N_{\rm H}$ when deriving the errors on the intrinsic luminosity. This is in fact the main source of uncertainty in $L_{\rm X}$, at least for obscured sources. We compared our results for the targets in the COSMOS field with those presented by Marchesi et al. (2016b), who performed X-ray spectral analysis for all the targets with more than 30 counts in the 0.5−7 keV band. Ten out of sixteen of our COSMOS targets were analyzed in Marchesi et al. (2016b), for which the comparison results in an average $\langle \log(L_{\rm X,\,literature}/L_{\rm X,\,this\,work})\rangle = -0.08$ dex and $\langle \log(N_{\rm H,\,literature}/N_{\rm H,\,this\,work})\rangle = 0.07$ dex, as well as a standard deviation of 0.2 and 0.3 dex, respectively.

The results derived for column densities and 2−10 keV absorption-corrected luminosities are listed in Table A.2. X-ray luminosities range between $L_{\rm X} = 1.6 \times 10^{43}$ erg s^{-1} and 6.5×10^{45} erg s^{-1}, therefore including AGN with Seyfert-like X-ray luminosities ($L_{\rm X} \sim 10^{42} - 10^{44}$ erg s^{-1}) and quasar-like ones ($L_{\rm X} > 10^{44}$ erg s^{-1}). In terms of column densities, the target sample covers uniformly a range from unobscured ($N_{\rm H} \leq 10^{20}$ cm^{-2}, given by the Galactic value) to obscured and Compton-thick AGN ($N_{\rm H} > 10^{24}$ cm^{-2}), with values up to 2×10^{24} cm^{-2}. For the objects whose column density derived from the X-ray spectral analysis is $\sim 10^{20}$ cm^{-2} we provide 90% confidence level upper limits. From an X-ray point of view, AGN are classified as unobscured when $N_H < 10^{22}$ cm^{-2} and obscured vice versa. Overall the sample is split in almost an equal number of unobscured and obscured objects based on the X-ray classification. Further discussion about these results, in relation to other physical properties of our targets, is presented in Sect. 4.2.

3. Target sample characterization

To draw a wide and complete picture of the physical properties of our AGN and host galaxies, a full multi-wavelength support is needed. We make use of the rich suite of multi-wavelength ancillary data available for these targets, which are unique in terms of amount and depth. They range from the X-rays (Sect. 2.1) to the optical, NIR and FIR regimes, and up to the radio (see Sect. 4.3). This allows us to gather information about AGN quantities, such as obscuring column density, X-ray and bolometric luminosity, BH mass, as well as galaxy ones, such as stellar mass and SFR.

In this Section we describe the ancillary data collected for this work from the UV to the FIR when available, as well as the code used to perform the SED-fitting analysis of the target sample.

3.1. Multi-wavelength dataset

The counterparts to the X-ray sources in the CDF-S and COSMOS are provided along with the optical-to-MIR multi-wavelength photometry by the original catalogs (Hsu et al. 2014; Laigle et al. 2016), where in both cases images were previously registered at the same reference and the photometry was PSF-homogenized. The counterparts to the SUPER targets in XMM-XXL and Stripe82X are known in the SDSS optical images and the corresponding associations to the X-ray sources are likewise given in the original catalogs (Fotopoulou et al. 2016; LaMassa et al. 2016; Ananna et al. 2017). The remaining SDSS targets are WISE selected with follow-up in the X-ray band (Martocchia et al. 2017).

We complemented the UV-to-MIR photometry with further FIR data from *Herschel*/PACS and SPIRE, when available, using a positional matching radius of 2″, taking into account that we used 24 μm-priored catalogs which in turn are IRAC-3.6 μm priored. Here we briefly describe the multi-wavelength data set used for this study but further information can be found in the specific papers mentioned for each field in the following. In Table 1 we summarize the wavelength bands used to build the SEDs of our AGN. The column description of the photometric catalog is available in Appendix B.

3.1.1. CDF-S

The multi-wavelength catalog used for this field, presented in Hsu et al. (2014), provides UV-to-MIR photometric data for all the sources detected in the Extended *Chandra* Deep Field-South (E-CDF-S; Xue et al. 2016; Lehmer et al. 2005), combining data from CANDELS (Guo et al. 2013), MUSYC (Cardamone et al. 2010) and TENIS (Hsieh et al. 2012). MIR and FIR photometry at 24 μm with *Spitzer*/MIPS and at 70, 100 and 160 μm with *Herschel*/PACS is presented by Magnelli et al. (2013), combining observations from the PACS Evolutionary Probe (PEP; Lutz et al. 2011) and the GOODS-*Herschel* programs (GOODS-H; Elbaz et al. 2011). *Herschel*/SPIRE fluxes at 250, 350 and 500 μm are taken from the *Herschel* Multi-tiered Extragalactic Survey (HerMES; Roseboom et al. 2010, 2012; Oliver et al. 2012) DR3. We point out that the HerMES team provides also *Herschel*/PACS photometry for the same field. However, we decided to take advantage of the deeper data released by the PEP team, after verifying the consistency of the fluxes obtained by both teams. Two out of the six targets in the CDF-S are outside the area covered by CANDELS (namely XID36 and XID57). Therefore, we adopted FIR observations at 100 and 160 μm from the PEP DR1 (Lutz et al. 2011), since the data products released by Magnelli et al. (2013) cover the GOODS-S field only. The prior information for these FIR catalogs is given by IRAC-3.6 μm source positions. To this data set, we added ALMA data in Band 7 and 3 available from the ALMA Archive and Scholtz et al. (2018).

3.1.2. COSMOS

The UV-to-MIR photometry is taken from the COSMOS2015 catalog presented in Laigle et al. (2016), combining existing data from previous releases (e.g., Capak et al. 2007; Ilbert et al. 2009, 2013) and new NIR photometry from the UltraVISTA-DR2 survey, *Y*-band observations from Subaru and infrared data from *Spitzer*. The source detection is based on deep NIR images and all the photometry is obtained from images registered at the same reference. *Spitzer*/MIPS photometry at 24 μm and *Herschel*/PACS at 100 and 160 μm is taken from the PEP DR1

Table 1. Summary of the photometric data used for the SED-fitting modeling.

Field	λ range	Reference	Telescope/Instrument	Bands
XMM-XXL	UV to MIR	Georgakakis et al. (2017) and	GALEX	NUV
		Fotopoulou et al. (2016)	CFHT	*u, g, r, i, z*
			SDSS	*u, g, r, i, z*
			VISTA	*z, Y, J, H, K*
			Spitzer/IRAC	3.6, 4.5, 5.8, 8.0 μm
		Lang et al. (2016)	WISE	*W1, W2, W3, W4*
	24−500 μm	Oliver et al. (2012)	*Spitzer*/MIPS	24 μm
			Herschel/PACS	70, 100, 160 μm
			Herschel/SPIRE	250, 350, 500 μm
CDF-S	UV to MIR	Hsu et al. (2014)	CTIO-Blanco/Mosaic-II	*U*
			VLT/VIMOS	*U*
			HST/ACS	F435W, F606W, F775W, F814W, F850LP
			HST/WFC3	F098M, F105W, F125W, F160W
			ESO-MPG/WFI	$UU_{38}BVRI$
			CTIO-Blanco/Mosaic-II	z-band
			NTT/SofI	H-band
			CTIO-Blanco/ISPI	*J, K*
			VLT/ISAAC	K_S
			VLT/HAWK-I	K_S
			Spitzer/IRAC	3.6, 4.5, 5.8, 8.0 μm
	24−160 μm	Magnelli et al. (2013) or	*Spitzer*/MIPS	24 μm
		Lutz et al. (2011)	*Herschel*/PACS	70, 100, 160 μm
	250−500 μm	Oliver et al. (2012)	*Herschel*/SPIRE	250, 350, 500 μm
	>1000 μm	Scholtz et al. (2018) and	ALMA	Band 7 (800−1100 μm)
		ALMA Archive		Band 3 (2600−3600 μm)
COSMOS	UV to MIR	Laigle et al. (2016)	GALEX	NUV
			CFHT/MegaCam	u^*
			Subaru/Suprime-Cam	*B, V, r,* i^+, z^{++},
			Subaru/HSC	*Y*
			VISTA/VIRCAM	*Y, J, H,* K_s
			CFHT/WIRCam	*H,* K_s
			Spitzer/IRAC	3.6, 4.5, 5.8, 8.0 μm
	24−160 μm	Lutz et al. (2011)	*Spitzer*/MIPS	24 μm
			Herschel/PACS	70, 100, 160 μm
	250−500 μm	Hurley et al. (2017)	*Herschel*/SPIRE	250, 350, 500 μm
	>1000 μm	Scholtz et al. (2018) and	ALMA	Band 7 (800−1100 μm)
		ALMA Archive		Band 3 (2600−3600 μm)
WISSH	UV to MIR	Duras et al. (in prep.)	SDSS	*u, g, r, i, z*
			2MASS	*J, H, K*
			WISE	*W1, W2, W3, W4*
Stripe 82X	UV to MIR	Ananna et al. (2017)	SDSS	*u, g, r, i, z*
			UKIDSS	*J, H, K*
			VISTA	*J, H, K*
			Spitzer/IRAC	3.6, 4.5 μm
		Lang et al. (2016)	WISE	*W1, W2, W3, W4*

(Lutz et al. 2011) extracted using IRAC-3.6 μm source position priors, as mentioned above. The 24 μm data for the targets cid_971 and lid_206 were provided by Le Floc'h (priv. comm.), since they are particularly faint in this band and therefore not reported in the original catalog. *Herschel*/SPIRE photometry at 250, 350 and 500 μm is retrieved from the data products presented in Hurley et al. (2017), who describe the 24 μm prior-based source extraction tool XID+, developed using a probabilistic Bayesian method. The resulting flux probability distributions for each source in the catalog are described by the 50th, 84th and 16th percentiles. We assumed Gaussian uncertainties by taking the maximum between the 84th–50th percentile and the 50th–16th percentile. As done for the CDF-S, we added ALMA data in Band 7 and 3 available from the ALMA Archive and Scholtz et al. (2018).

3.1.3. XMM-XXL North

The multi-wavelength photometry from UV-to-MIR for this field is obtained by merging the photometric SDSS and CFHTLenS (Erben et al. 2013) optical catalogs (see Fotopoulou et al. 2016; Georgakakis et al. 2017). These data were complemented with GALEX/NUV photometry, *YZJHK* band photometry from VISTA as well as *u* and *i* bands from CFHT (see Fotopoulou et al. 2016). We considered total magnitudes for CFHTLenS data and model mag for SDSS. As for IRAC, we

considered aperture 2 (1.9″) photometry corrected to total. The WISE data are taken from Lang et al. (2016), who provide forced photometry of the WISE All-sky imaging at SDSS positions. *Herschel*/PACS and SPIRE data are those released by the HerMES collaboration in the Data Release 4 and 3 respectively (Oliver et al. 2012). Both sets of data are extracted using the same *Spitzer*/MIPS 24 μm prior catalog, whose fluxes are available along with the SPIRE data. We use aperture fluxes in smaller apertures, that is 4″ diameter.

3.1.4. Stripe82X

We used the photometry that was made public in Ananna et al. (2017) and was used for the computation of the photometric redshifts in the field. The data are homogeneously deep in optical (Fliri & Trujillo 2016), but in the NIR and MIR a patchwork of surveys was used (see Ananna et al. 2017, and its Fig. 1). Similarly to the XMM-XXL photometry, we took WISE data from Lang et al. (2016).

3.1.5. WISSH

For these targets we collected UV-to-MIR photometry from the WISSH photometric catalog (Duras et al., in prep.), which includes SDSS photometry, NIR data from the 2MASS as well as WISE photometry from 3 to 22 μm (see Duras et al. 2017, for further details).

All the data used in this work are corrected for Galactic extinction (Schlegel et al. 1998). The resulting photometry, from NUV to FIR, spans a maximum of 31, 36, 27, 12 and 17 wavebands overall for XMM-XXL, CDF-S, COSMOS, WISSH and Stripe82X, respectively. However there is some overlap among bands from different surveys, which reduces the number of unique wavebands. As far as the mid and far-IR photometry from 24 to 500 μm is concerned, we considered as detections only photometric points with $S/N > 3$, where the total noise is given by the sum in quadrature of both the instrumental and the confusion ones (Lutz et al. 2011; Oliver et al. 2012; Magnelli et al. 2013). The detections below this threshold were converted to 3σ upper limits. The number of targets with ($\geq$3σ) *Herschel* detections in at least one PACS band is 7 out of 39, while there are 12 out of 39 targets with at least one SPIRE band detection. Five sources present detections in both PACS and SPIRE filters. All the targets have photometric data available from the UV to the MIR.

Although these data enable a detailed SED modeling, they are collected and/or stacked over many years, so that issues related to variability (intrinsic properties of AGN) can potentially arise (e.g., Simm et al. 2016). While we cannot correct for variability in case of stacked images, we were able to correct this issue for the AGN whose photometry was taken in the same wavebands from different surveys. Clear variability was shown by the XMM-XXL targets X_N_4_48, X_N_35_20 and X_N_44_64, for which the SDSS photometry was brighter than the CFHT one by up to two magnitudes. We have taken the latter since it is closer in time to the X-ray observations.

3.2. Data modeling

The analysis presented in this work is performed by using the Code Investigating GALaxy Emission (CIGALE[4]; Noll et al. 2009), a publicly available state-of-the-art galaxy SED-fitting technique. CIGALE adopts a multi-component fitting approach in order to disentangle the AGN contribution from the emission of its host galaxy and estimate in a self-consistent way AGN and host galaxy properties from the integrated SEDs. Moreover, it takes into account the energy balance between the UV-optical absorption by dust and the corresponding re-emission in the FIR. Here we provide a brief description of the code and we refer the reader to Noll et al. (2009), Buat et al. (2015) and Ciesla et al. (2015) for more details. In this work we used the version 0.11.0.

CIGALE accounts for three main distinct emission components: (i) stellar emission, dominating the wavelength range 0.3−5 μm; (ii) emission by cold dust heated by star formation which dominates the FIR; (iii) AGN emission, appearing as direct energy coming from the accretion disk at UV-optical wavelengths and reprocessed emission by the dusty torus peaking in the MIR. The code assembles the models, according to a range of input parameters, which are then compared to the observed photometry by computing model fluxes in the observed filter bands and performing an evaluation of the χ^2. The output parameters as well as the corresponding uncertainties are determined through a Bayesian statistical analysis: the probability distribution function (PDF) for each parameter of interest is built by summing the exponential term $\exp(-\chi^2/2)$ related to each model in given bins of the parameter space. The output value of a parameter is the mean value of the PDF and the associated error is the standard deviation derived from the PDF (Noll et al. 2009). The values of the input parameters used for the fitting procedure are listed in Table 2. In the following we describe the assumptions and the models adopted.

(i) To create the stellar models we assumed a star formation history (SFH) represented by a delayed τ-model (exponentially declining) with varying e-folding time and stellar population ages (see Table 2), defined as:

$$\mathrm{SFR}(t) \propto t \times \exp(-t/\tau) \quad (1)$$

where τ is the e-folding time of the star formation burst. The stellar population ages are constrained to be younger than the age of the Universe at the redshift of the source sample. The SFH is then convolved with the stellar population models of Bruzual & Charlot (2003) and a Chabrier (2003) initial mass function (IMF). The metallicity is fixed to solar (0.02)[5]. To account for the role played by dust in absorbing the stellar emission in the UV/optical regime we applied an attenuation law to the stellar component. One of the most used ones, also at high redshift, is the Calzetti et al. (2000) law. However, in the literature there is evidence for shapes of the attenuation law different from the standard Calzetti one (e.g., Salvato et al. 2009; Buat et al. 2011, 2012; Reddy et al. 2015; Lo Faro et al. 2017, but see also Cullen et al. 2018). We used the modified version of the Calzetti et al. (2000) curve, which is multiplied in the UV range by a power law with a variable slope δ, where the attenuation is given by $A(\lambda) = A(\lambda)_{\mathrm{Calz.}} \times (\lambda/550\,\mathrm{nm})^{\delta}$. In this recipe, negative slopes of the additional power law produce steeper attenuation curves and vice versa positive values give a flatter curve, while a slope equal to 0 reproduces the Calzetti et al. (2000) curve. We did not include the bump feature at 2175 Å. The same law is applied to both old (>10 Myr) and young (<10 Myr; Charlot & Fall 2000) stars. Moreover we took into account that stars of different ages can suffer from differential

[4] https://cigale.lam.fr

[5] The impact of lower metallicity on the SED-fitting output was tested by fixing the metallicity to a value 0.3 dex lower than the solar one. The results of the fitting procedure are well within the uncertainties.

Table 2. Input parameter values used in the SED-fitting procedure.

Template	Parameter	Value and range	Description
Stellar emission	IMF	Chabrier (2003)	
	Z	0.02	Metallicity
	Separation age	10 Myr	Separation age between the young and the old stellar populations
Delayed SFH	Age	0.10, 0.25, 0.5, 1.0, 1.5, 2.0, 2.5 Gyr	Age of the oldest SSP
	τ	0.10, 0.25, 0.5, 1.0, 3.0, 5.0, 10.0 Gyr	e-folding time of the SFH
Modified Calzetti	$E(B-V)$	0.05, 0.1, 0.3, 0.5, 0.7, 0.9, 1.1, 1.3	Attenuation of the young stellar population
attenuation law	Reduction factor	0.93	Differential reddening applied to the old stellar population
	δ	–0.6, –0.4, –0.2, 0.0	Slope of the power law multiplying the Calzetti attenuation law
Dust emission	$\alpha_{\rm SF}$	0.5, 1.0, 1.5, 2.0, 2.5, 3.0	Slope of the power law combining the contribution of different dust templates
AGN emission	$R_{\rm max}/R_{\rm min}$	60	Ratio of the outer and inner radii
	$\tau_{9.7}$	0.6, 3.0, 6.0	Optical depth at 9.7 μm
	β	0.00, –0.5, –1.0	Slope of the radial coordinate
	γ	0.0, 6.0	Exponent of the angular coordinate
	Θ	100 deg	Opening angle of the torus
	ψ	0, 10, 20, 30, 40, 50, 60, 70, 80, 90 deg	Inclination of the observer's line of sight
	$f_{\rm AGN}$	0.05, 0.1, 0.15, 0.2, 0.25, 0.3, 0.35, 0.4, 0.45, 0.5, 0.55, 0.6, 0.65, 0.7, 0.75, 0.8, 0.85, 0.9	AGN fraction
Nebular emission	U	10^{-2}	Ionization parameter
	$f_{\rm esc}$	0%	Fraction of Lyman continuum photons escaping the galaxy
	$f_{\rm dust}$	10%	Fraction of Lyman continuum photons absorbed by dust

reddening by applying a reduction factor of the visual attenuation to the old stellar population (Calzetti et al. 2000). The reduction factor, $E(B-V)_{\rm old}/E(B-V)_{\rm young}$, is fixed to 0.93 as derived by Puglisi et al. (2016).

(ii) The reprocessed emission from dust heated by star formation is modeled using the library presented by Dale et al. (2014), which includes the contributions from dust heated by both star formation and AGN activity. In order to treat the AGN emission separately by adopting different models, and therefore estimate the contribution from star formation only with this library, we assumed an AGN contribution equal to 0. This family of models is made of a suite of templates constructed with synthetic and empirical spectra which represent emission from dust exposed to a wide range of intensities of the radiation field. These templates are combined in order to model the total emission and their relative contribution is given by a power law, whose slope is the parameter $\alpha_{\rm SF}$. For higher values of the slope the contribution of weaker radiation fields is more important and the dust emission peaks at longer wavelengths. The dust templates are linked to the stellar emission by a normalization factor which takes into account the energy absorbed by dust and re-emitted in the IR regime.

(iii) Accounting for the AGN contribution is essential for the determination of the host galaxy properties. To reproduce the AGN emission component we chose the physical models presented by Fritz et al. (2006), who solved the radiative transfer equation for a flared disk geometry with a smooth dust distribution composed by silicate and graphite grains. Although a clumpy or filamentary structure has been observed for nearby AGN (e.g., Jaffe et al. 2004) and is more physical, in this work we focus on the global characterization of the SED, for which both clumpy and smooth models provide good results and are widely used in the literature. As claimed by Feltre et al. (2012), the major differences in the SEDs produced by the two dust distributions are due to different model assumptions and not to their intrinsic properties. The main AGN parameter we want to reliably constrain from the SED is the AGN bolometric luminosity, therefore the details of the dust distribution are not fundamental in this work. The law describing the dust density within the torus is variable along the radial and the polar coordinates and is given by:

$$\rho(r,\theta) = \alpha r^{\beta} e^{-\gamma|\cos(\theta)|} \quad (2)$$

where α is proportional to the equatorial optical depth at 9.7 μm ($\tau_{9.7}$), β and γ are related to the radial and angular coordinates respectively. Other parameters describing the geometry are the ratio between the outer and the inner radii of the torus, $R_{\rm max}/R_{\rm min}$, and the opening angle of the torus, Θ. The inclination angle of the observer's line of sight with respect to the torus equatorial plane, the parameter ψ with values in the range between 0° and 90°, allows one to distinguish between type 1 AGN (unobscured) for high inclinations and type 2 AGN (obscured) for low inclinations. Intermediate types are usually associated to $\psi \simeq 40°-60°$ depending on the dust distribution. The central engine is assumed to be a point-like source emitting isotropically with an SED described by a composition of power laws parameterizing the disk emission. This emission is partially obscured when the line of sight passes through the dusty torus. Another important input parameter that handles the normalization of the AGN component to the host galaxy emission is the AGN fraction, which is the contribution of the AGN emission to the total (8−1000 μm) IR luminosity and is given by $f_{\rm AGN} = L_{\rm IR}^{\rm AGN}/L_{\rm IR}^{\rm TOT}$, with $L_{\rm IR}^{\rm TOT} = L_{\rm IR}^{\rm AGN} + L_{\rm IR}^{\rm starburst}$ (Ciesla et al. 2015). The input values available in the code are based on the results presented by Fritz et al. (2006). However, as described by Hatziminaoglou et al. (2008), using all the

possible values would produce degeneracies in the model templates. Therefore we cannot determine the torus geometry in an unequivocal way and the parameter proving to be best constrained is the bolometric luminosity. The values of the above-mentioned physical parameters related to the torus geometry should be taken as indicative. For this reason we decided to narrow down the grid of input values and to fix some of them. Our selected values (see Table 2) are partly based on the analysis performed by Hatziminaoglou et al. (2008), who presented a restricted grid of input parameters. Differently from their setup, we fixed $R_{\rm max}/R_{\rm min}$ and the opening angle to a single value, as well as using a less dense grid for the optical depth.

To the main emission components described above we also added templates reproducing nebular emission, ranging from the UV to the FIR. These templates are based on the models presented by Inoue (2011) and represent the emission from H II regions. They include recombination lines, mainly from hydrogen and helium, and continuum emission due to free-free, free–bound and 2-photon processes of hydrogen. This SED component is proportional to the rate of Lyman continuum photons ionizing the gas and takes into account the Lyman continuum escape fraction and the absorption of the ionizing photons by dust. The templates do not include lines from photo-dissociation regions and nebular lines due to AGN emission. Therefore they do not reproduce the AGN contribution to the emission lines which may contaminate the photometric data. We fixed the parameters of the nebular emission model (see Table 2) as in Boquien et al. (2016).

4. Overall properties of the target sample

In this section we provide a detailed picture of the multi-wavelength properties of our target sample obtained using SED fitting and spectral analysis. In particular, we focus on the main AGN and host galaxy physical parameters that we aim to connect to the outflow properties, as traced by our on-going SINFONI observations.

The AGN sample is characterized by a wide range of column densities, up to 2×10^{24} cm^{-2}, derived from the X-ray spectra (see Sect. 2.2). This translates into different levels of contamination of the AGN to the galaxy emission at UV-to-NIR wavelengths. Therefore, host galaxy properties for the targets where this contamination is low, that is obscured AGN, can be robustly determined. At the same time, AGN properties are better constrained for unobscured targets, whose emission prevails in the UV-to-IR portion of the SED. In general, the classification of AGN into obscured and unobscured sources can be performed based on different criteria, such as X-ray spectral analysis, optical spectral properties, and shape of the UV-to-NIR SED (see Merloni et al. 2014). We adopt the following nomenclature: from an optical point of view, the classification depends on the presence of broad (FWHM > 1000 km s^{-1}) or narrow (FWHM < 1000 km s^{-1}) permitted lines in their spectra, defining broad-line (BL) or narrow-line (NL) AGN respectively; according to the shape of the UV-to-NIR SED, we can constrain the AGN type based on the inclination of the observer's line of sight with respect to the obscuring torus; finally, AGN are classified as unobscured or obscured when the column density is smaller or larger than 10^{22} cm^{-2} (see Sect. 2.2). As explained later in Sect. 4.2, the three classification methods broadly agree with each other. However, as final classification, we decided to adopt the optical spectroscopic classification (BL/NL, Table A.2). In the following we will refer to type 1 and type 2 AGN as based on the optical spectroscopic classification.

4.1. SED-fitting results

The main output parameters obtained with CIGALE are reported in Table A.2, that is stellar mass, SFR, and AGN bolometric luminosity together with their 1σ uncertainties. Two representative examples of SEDs are shown in Fig. 2 for a type 2 (left panel) and a type 1 (right panel) AGN from CDF-S and COSMOS, respectively. The SEDs of the whole sample are presented in Appendix C.

4.1.1. Stellar masses

Stellar masses (M_*) are probed by rest-frame NIR flux densities shifted to the MIR at this redshift, which are dominated by old stellar populations. The uncertainty associated to stellar masses increases with the level of AGN contamination. As shown by the green template in the left panel of Fig. 2, in type 2s there is a negligible AGN contribution in the UV-to-NIR regime. Conversely, for type 1s the green template in the right panel outshines the galaxy emission (orange curve) preventing a derivation of the stellar mass as robust as for type 2s. However, estimates of the stellar mass for type 1 AGN can still be recovered albeit with larger uncertainties (e.g., Bongiorno et al. 2012), apart from very bright type 1s (e.g., Stripe82X, WISSH and some XMM-XXL targets in our sample) for which the uncertainties on this parameter are much larger than the parameter value itself and therefore an estimate of the stellar mass is meaningless. For these targets, we do not report a value of M_* in Table A.2. Our results range between $\sim 4 \times 10^9\ M_\odot$ and $\sim 1.6 \times 10^{11}\ M_\odot$, with an average 1σ uncertainty of 0.1 dex for type 2s and 0.3 dex for type 1s[6].

4.1.2. Star formation rates

SFRs are derived from the IR luminosity integrated in the rest-frame wavelength range 8−1000 μm, when possible, assuming the Kennicutt (1998b) SFR calibration converted to a Chabrier (2003) IMF (i.e., by subtracting 0.23 dex). This value is an indication of the SFR averaged over the last 100 Myr of the galaxy history and is produced by emission from dust heated by young stars as well as from evolved stellar populations. The AGN also contributes to the IR luminosity (whose percentage is given by the AGN fraction, see Sect. 3.2), although it usually dominates the emission only up to 30 μm rest-frame as described in Mullaney et al. (2011) (see also Symeonidis et al. 2016). Since our SED fitting allows us to disentangle the contribution of the two components (AGN and SF), we estimate the IR luminosity from SF removing the AGN contamination[7]. However this is affected by intrinsic degeneracies that cannot be solved with the current data sampling at MIR and FIR wavelengths. Therefore an over-estimation of the AGN fraction will result in an under-estimation of the IR emission from the galaxy and thus of the SFR and vice versa (e.g., Ciesla et al. 2015). We provide a 3σ upper limit on the SFR, derived as the 99.7th percentile of the FIR luminosity PDF, for the targets with only upper limits at $\lambda > 24\,\mu$m. For the subset of targets without data at observed

[6] In general, the statistical uncertainties in the determination of M_* and SFR through SED modeling are typically around 0.3 dex for stellar masses and larger for SFRs (e.g., Mancini et al. 2011; Santini et al. 2015), usually underestimated by the SED-fitting tools. Moreover, systematic differences in the results are due to the models used, degeneracies and a priori assumptions as well as the discrete coverage of the parameter space.

[7] AGN fractions (derived for the targets with FIR detections) range between 0.05 and 0.90, with a median value of 0.36.

$\lambda > 24\,\mu$m we did not include the dust templates in the fitting procedure. Therefore we report the average SFR over the last 100 Myr of the galaxy history as obtained from the modeling of the stellar component in the UV-to-NIR regime with SED fitting. This has been done for cid_971 and lid_206, since their $24\,\mu$m flux was not available in the catalog used as a prior for the extraction of the FIR photometry (see Sect. 3.1). The targets without an estimate of the SFR are instead bright type 1s, therefore no information about SFR, and stellar mass, can be retrieved from the UV-optical regime. SFRs determined for our targets are in the range between $\sim 25\,M_{\odot}\,\mathrm{yr}^{-1}$ and $\sim 680\,M_{\odot}\,\mathrm{yr}^{-1}$ with an average 1σ uncertainty of 0.15 dex for type 1 and 0.06 for type 2 AGN (see footnote 6). The SFRs derived from the FIR luminosity and through the modeling of the stellar emission in the UV-to-NIR regime are in very good agreement (when the comparison is possible), with the low scatter due to the energy-balance approach used (see also Bongiorno et al. 2012).

4.1.3. Comparison of M_* and SFRs to literature results

We compared our results with those presented by Santini et al. (2015) for the targets in the CDF-S and Chang et al. (2017), Delvecchio et al. (2017) as well as Suh et al. (2017) for the COSMOS targets. Santini et al. (2015) collected M_* measurements of the targets in the CANDELS field from several teams which used different SED-fitting codes and assumptions, in order to study the influence of systematic effects on the final output. The resulting estimates turned out to be clustered around the median value with a scatter of 25%−35%. Their results are available for all of our CDF-S targets covered by CANDELS. Chang et al. (2017) derived physical parameters for galaxies over the whole COSMOS field, Delvecchio et al. (2017) dealt with a sub-sample of AGN as part of the VLA-COSMOS 3 GHz Large Project, while Suh et al. (2017) provided physical properties for a sample of X-ray selected type 2s. 16, 6 and 7 out of 16 of our COSMOS targets have a match in these catalogs, respectively. However, the values from Delvecchio et al. (2017) have been recomputed by adopting the same photometry used in this work (Delvecchio, priv. comm.). The overall comparison for stellar masses is quite satisfactory, with the average $\langle \log(M_{*,\,\mathrm{literature}}/M_{*,\,\mathrm{this\ work}})\rangle$ equal to 0.30 dex (this result includes both type 2 and type 1 AGN), 0.03 dex and 0.18 dex for Chang et al. (2017), Delvecchio et al. (2017) and Suh et al. (2017), and 0.20 dex for Santini et al. (2015). The standard deviation is 0.38, 0.3 and 0.19 dex for the COSMOS targets and 0.19 dex for the CDF-S ones. The fits performed in Santini et al. (2015) do not take into account the AGN contribution. As for the SFRs, the results are similar, with an average $\langle \log(\mathrm{SFR}_{\mathrm{literature}}/\mathrm{SFR}_{\mathrm{this\ work}})\rangle = 0.39$, –0.30 and 0.03 dex and standard deviation 0.44, 0.34 and 0.47 dex for Chang et al. (2017), Delvecchio et al. (2017) and Suh et al. (2017), respectively. The AGN contribution was subtracted in all the estimates. For this comparison we did not consider the SFRs reported in Santini et al. (2015), because their SED fitting did not include the FIR fluxes which are crucial to properly constrain the total SFR. The larger discrepancies for SFRs are mainly attributed to different and looser constraints in the FIR regime. In general, other sources of uncertainties are the diverse models used and the sparser data with large error bars (often just upper limits) compared to the UV-to-NIR regime.

Although the SFR is a key quantity to be compared with AGN activity in order to understand the feedback processes, measuring the current SFR in AGN hosts is a well-known challenge, since the tracers are usually contaminated by AGN emission. Thanks to the SINFONI data that will be available for our targets, we will be able to compare various SF tracers (e.g., narrow Hα vs. L_{FIR}) in order to explore the systematic effects in this kind of measurements.

4.1.4. AGN bolometric luminosities

As described in Sect. 3.2, we used the Fritz et al. (2006) models to reproduce the overall AGN emission. According to a comparison discussed in Ciesla et al. (2015), type 2 AGN templates from the Fritz et al. (2006) library are cooler than the SEDs obtained empirically by Mullaney et al. (2011), which may indicate that those models do not reproduce all the physical properties of the AGN obscuring structure. Moreover, there are several models (both theoretical and empirical) in the literature reproducing the dusty torus emission (e.g., Nenkova et al. 2008; Mor & Netzer 2012; Stalevski et al. 2012; Lani et al. 2017) and approximations of the intrinsic AGN continuum (e.g., Telfer et al. 2002; Richards et al. 2006; Stevans et al. 2014). Nevertheless, it is important to stress that our main goal is not the detailed determination of the torus or accretion disk specific characteristics but just recovering the AGN bolometric luminosity. To test the reliability of the derived quantity we explored the input parameter space described in Sect. 3.2 (see also Table 2) by fixing the input parameters to different values and comparing L_{bol} to those obtained using the whole grid of models used in this work. Even though the best-fit geometry varied through the different runs, the bolometric luminosity proved to be constrained within a variation of 0.2 dex. The same trend emerged for the dust luminosity due to star formation, which is related to the AGN luminosity by the AGN fraction. Moreover, we compared our results with available literature values for the targets in the COSMOS field (from Chang et al. 2017; Delvecchio et al. 2017) and those from the WISSH catalog (Duras, priv. comm.; Duras et al. 2017). Duras et al. (2017) modeled the AGN emission combining models from Feltre et al. (2012) and Stalevski et al. (2016); Chang et al. (2017) used empirical templates by Richards et al. (2006), Polletta et al. (2007), Prieto et al. (2010) and Mullaney et al. (2011); Delvecchio et al. (2017) adopted the Feltre et al. (2012) library. In spite of the variety of models used by the different authors, the comparison is satisfactory and all the results are within 0.3 dex scatter: the average $\langle \log(L_{\mathrm{bol,\,literature}}/L_{\mathrm{bol,\,this\ work}})\rangle$ is equal to 0.03, 0.18 and –0.09 dex for Chang et al. (2017), Delvecchio et al. (2017) and Duras (priv. comm.) respectively, with standard deviation 0.26, 0.30 and 0.14 dex. From our SED fitting, average 1σ uncertainties of the bolometric luminosity are on the order of 0.03 and 0.1 dex for type 1s and type 2s respectively, with best-fit values in the range 2×10^{44}–$8 \times 10^{47}\,\mathrm{erg\,s^{-1}}$. As pointed out for M_* and SFRs, the uncertainties estimated through SED fitting can be underestimated. According to the comparison mentioned above, a more realistic typical uncertainty can be fixed to 0.3 dex.

The physical quantities available for the SUPER sample give us the opportunity to study the distribution of the X-ray bolometric correction in the hard 2−10 keV band (defined as $k_{\mathrm{bol,\,X}} = L_{\mathrm{bol}}/L_{[2-10\,\mathrm{keV}]}$) versus L_{bol}. This can be done over a wide range of bolometric luminosities with a set of values determined in a uniform way. In Fig. 3 we compare our results to the relation derived by Lusso et al. (2012) for a sample of more than 900 AGN (both type 1 and type 2) selected from the COSMOS field (see also Lusso & Risaliti 2016). At variance with their AGN selection, which includes sources with hard X-ray fluxes larger than $3 \times 10^{-15}\,\mathrm{erg\,s^{-1}\,cm^{-2}}$, 23% of our targets reach fainter values (down to $\sim 5 \times 10^{-17}\,\mathrm{erg\,s^{-1}\,cm^{-2}}$, triangles in Fig. 3). Moreover, we can probe the $k_{\mathrm{bol,\,X}} - L_{\mathrm{bol}}$ relation for targets

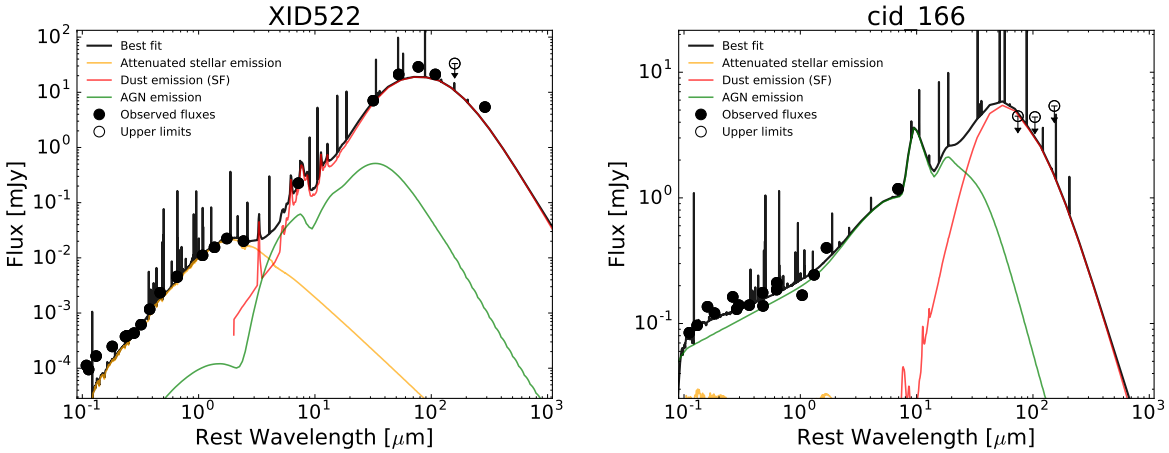

Fig. 2. Two examples of rest-frame SEDs obtained for a type 2 (XID522, *left*) and a type 1 (cid_166, *right*) AGN. The black dots represent the observed multi-wavelength photometry, while the empty dots indicate 3σ upper limits. The black solid line is the total best-fit model, the orange curve represents the stellar emission attenuated by dust, the green template reproduces the AGN emission, the red curve accounts for dust emission heated by star formation. Emission lines in the black curves are part of the nebular emission component, included in the overall SED.

with bolometric luminosities an order of magnitude higher (see also Martocchia et al. 2017). We plot the relations obtained by Lusso et al. (2012) for type 1 and type 2 AGN (solid and dashed lines respectively), although they do not differ too much. The shaded areas depict the dispersion of these relations, while the red and blue squares represent the sample of type 1 and type 2 AGN, respectively, from which the relations were obtained. Our results for both type 1 (shown in red) and type 2 (shown in blue) are well consistent with the trends found by Lusso et al. (2012) with only the presence of three targets outside the $\pm1\sigma$ scatter, according to the error bars. The rest of the SUPER targets are within the scatter shown by their sample and also the most luminous AGN are well represented by those curves. One of the outliers has faint hard-band flux (marked by different symbols to distinguish the targets below the threshold adopted by Lusso et al. 2012) and a total number of X-ray counts <60. We note that the error bars in the plot are given by the error on $L_{\rm bol}$ provided by the SED-fitting code. In the upper-left corner of the panel we plot a median error bar taking into account a systematic error of 0.3 dex on $L_{\rm bol}$ which is more representative. Accounting for the scatter of the data presented by Lusso et al. (2012) around the best fits and the underestimated error bars for our $L_{\rm bol}$, our estimates result to be in agreement with the literature trends and therefore we can consider $L_{\rm bol}$ and $L_{\rm X}$ obtained with our analysis reliable parameters.

Bolometric luminosities can be also combined with black hole masses, when available, in order to obtain the Eddington ratio $\lambda_{\rm Edd} = L_{\rm bol}/L_{\rm Edd}$, where $L_{\rm Edd} = 1.5\times10^{38}(M_{\rm BH}/M_{\odot})$ erg s^{-1}. BH masses for type 1 AGN, ranging between 8×10^{7} and 1.6×10^{10} $M_{\odot}$, are reported in Table A.2 together with the respective references. These values are derived via the "virial method" mainly using the broad C IV λ1549 emission line and the calibration of Vestergaard & Peterson (2006). Such method is affected by well-known limitations since the C IV emitting gas could be affected by non-virial motion (Trakhtenbrot & Netzer 2012). However, in the present paper we only want to give a broad idea of the coverage in the $\lambda_{\rm Edd} - M_{\rm BH}$ plane that will be provided by our survey. As shown in Fig. 4, where we plot the distribution of BH masses and Eddington ratios, we will be able to sample both accretion rates close to the Eddington limit and more moderate ones ($\sim10^{-2}$ the Eddington limit) and to connect these quantities to the potential outflows that will be detected by SINFONI. To take into account the heavy uncertainties C IV-based BH mass estimates are affected by, we assume in Fig. 4 a systematic error on $M_{\rm BH}$ equal to 0.4 dex and plot a median error bar as a reference. Importantly, SINFONI observations will allow us to derive accurate estimates of $M_{\rm BH}$ combining broad Hβ and Hα line profiles with continuum luminosities verifying, and improving upon, the C IV-based measurements.

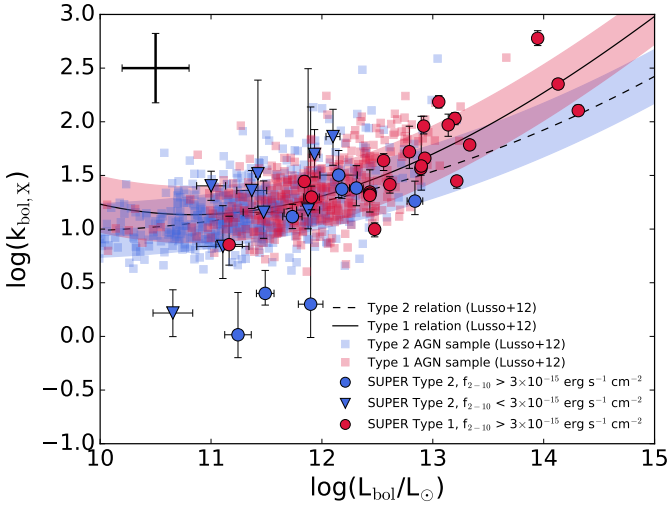

Fig. 3. Bolometric corrections in the hard 2−10 keV band versus bolometric luminosities. Circles and triangles mark the SUPER targets with 2−10 keV fluxes higher and lower than 3×10^{-15} erg s^{-1} cm^{-2} respectively, while type 1 and type 2 AGN are plotted in red and blue. The solid and dashed lines show the relations obtained by Lusso et al. (2012) for type 1s and type 2s with fluxes higher than 3×10^{-15} erg s^{-1} cm^{-2}, respectively. The shaded areas depict the scatter of these relations. We plot as red and blue squares the sample of type 1 and type 2 AGN, respectively, analyzed by Lusso et al. (2012) to show the dispersion of the data around the best-fit relations. The error bar in the upper-left corner takes into account a systematic error of 0.3 dex on $L_{\rm bol}$. The SUPER data points are well consistent with the trends found for the bolometric correction.

4.1.5. Comparison to the main sequence of star-forming galaxies

In Fig. 5 we show the location of our targets in the SFR-M_{*} plane for the objects with an estimate of both parameters, that is obscured AGN and a subsample of unobscured ones (24 targets,

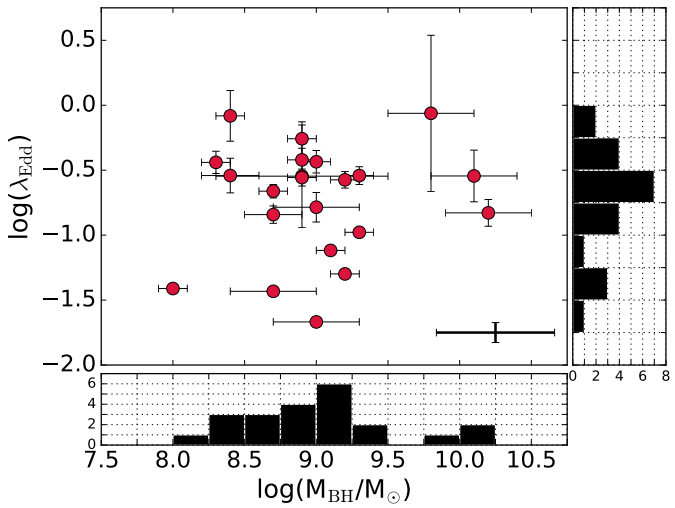

Fig. 4. Eddington ratios versus BH masses of the 22 type 1 AGN in the target sample. The Eddington ratio is given by $\lambda_{\rm Edd} = L_{\rm bol}/L_{\rm Edd}$, with bolometric luminosities estimated through SED-fitting analysis. BH masses (given in Table A.2) are derived via the "virial method" mainly using the broad C IV emission line and the calibration of Vestergaard & Peterson (2006). We plot a representative error bar at the bottom-right corner of the plot which takes into account a systematic error of 0.4 dex on $M_{\rm BH}$. The black histograms show the projected distribution of the two quantities along each axis. SUPER will allow us to sample both accretion rates close to the Eddington limit and more moderate ones and to connect these quantities to the potential outflows detected by SINFONI.

those for which we provide M_* and SFR in Table A.2). SFRs are already corrected for the AGN contribution. The distribution of our targets is compared to the so-called main sequence of star-forming galaxies (e.g., Noeske et al. 2007). We adopted the parametrization derived by Schreiber et al. (2015), who performed a stacking analysis of deep *Herschel* data in several extragalactic fields (GOODS, UDS, COSMOS), finding a flattening of the MS at high stellar masses ($\log(M_*/M_\odot) > 10.5$) and a SFR dispersion of 0.3 dex. Our sample covers in a quite uniform way the SFR-M_* plane, probing a wide range in terms of SFRs. About 46% of the targets are within the $\pm1\sigma$ scatter of the main sequence at the average redshift of the sample $z \sim 2.3$, while the rest are subdivided above (33%) and below (20%) it. As far as the stellar mass range is concerned, our AGN reside in massive hosts (median M_* of $10^{10.88}\,M_\odot$). This can be ascribed to a selection effect, as already pointed out by Bongiorno et al. (2012) and Aird et al. (2012). In particular, they found that AGN with a low Eddington ratio are more numerous than AGN with a high one. At a fixed X-ray flux limit there is a bias toward galaxies hosting an AGN with higher stellar masses, given the relation between $L_{\rm Edd}$, $M_{\rm BH}$ and M_*. Over a sample of 1700 AGN in the COSMOS field analyzed by Bongiorno et al. (2012), the host galaxy masses range from 10^{10} to $10^{11.5}\,M_\odot$, with a peak at $\sim10^{10.9}\,M_\odot$. The color coding in Fig. 5 refers to the AGN bolometric luminosity of each target. The detailed analysis of potential outflows in our AGN, as a function of their position in the SFR$-M_*$ plane and their bolometric luminosity, will expand the physical understanding of the impact of AGN outflows on host galaxies by investigating the variation of outflow properties (such as mass outflow rates and energetics) moving from above to below the MS.

Currently the largest AO-assisted NIR IFS observations of galaxies in the same redshift range covered by SUPER is represented by the SINS/zC-SINF survey (Förster Schreiber et al. 2018). These observations focus on the Hα and [N II] emission lines, probing their distribution and kinematics in the galaxy, with a spatial resolution of ~1.5 kpc. Excluding objects classified as AGN in Förster Schreiber et al. (2018), this SINFONI survey includes 25 objects, shown in Fig. 5, in the redshift range $2 < z < 2.5$ of the SUPER sample. The total stellar mass and SFR intervals, used to match the SINS/zC-SINF sample to the SUPER one, span a range which takes into account also the uncertainties on these quantities. As can be seen from Fig. 5, the SUPER and SINS/zC-SINF (excluding AGN) samples have an overlap in this plane, in the stellar mass range $\log(M_*/M_\odot) = [9.5{-}10.8]$, which will enable an interesting comparison of the properties of galaxies hosting active and inactive SMBHs.

4.2. X-ray vs. optical spectroscopic and SED-fitting classification

In Fig. 6 we plot the distribution of our targets in the AGN bolometric luminosity and column density plane. The coverage of this parameter space is quite uniform. The bolometric luminosity probed by our survey ranges from $\sim10^{44}\,{\rm erg\,s^{-1}}$ up to $\sim10^{48}\,{\rm erg\,s^{-1}}$, spanning almost 4 orders of magnitude. In terms of column density, the sample covers uniformly a range from unobscured ($N_{\rm H} \leq N_{\rm H}^{\rm gal}$) to heavily obscured objects, with values up to $2\times10^{24}\,{\rm cm^{-2}}$. We adopt a separation value of $10^{22}\,{\rm cm^{-2}}$ between obscured and unobscured AGN (Mainieri et al. 2002; Szokoly et al. 2004). In Fig. 6 we also compare the X-ray and optical (spectroscopy and SED fitting) diagnostics to distinguish between obscured and unobscured AGN as introduced at the beginning of Sect. 4. The diagnostic recovered from the SED fitting is the inclination of the observer's line of sight with respect to the torus equatorial plane, shown by the color coding in Fig. 6. The optical spectroscopic diagnostic (i.e., the presence of broad or narrow lines in the spectra) is depicted with different markers for broad- and narrow-line AGN. As can be clearly seen in Fig. 6, the three diagnostics agree rather well. Upper limits refer mainly to objects for which the column density derived from the X-ray spectral analysis is consistent with $\sim10^{20}\,{\rm cm^{-2}}$ (given by Galactic absorption) and are therefore classified as unobscured from an X-ray point of view, even if the formal upper limit for $N_{\rm H}$ is larger than $10^{22}\,{\rm cm^{-2}}$. In some cases, the SED-fitting procedure is affected by significant degeneracies, since the same SED can sometimes be fit by either a type 1 AGN template and a negligible contribution from the host galaxy or an absorbed AGN template together with a very young and UV-bright set of stellar populations. In most cases the results of the SED fitting were in agreement with the overall classification of the target, returning a robust estimate of the AGN type. For some of the bright (type 1) AGN we restricted the range of inclinations based on the obscuration type suggested by the spectroscopic diagnostic in order to overcome the degeneracy. There are also some ambiguous cases. We find 2 targets classified as unobscured in the X-rays but showing obscured characteristics in the optical regime (both in the spectra and in the SEDs), although the upper error for $N_{\rm H}$ is very large. Six targets show an obscured X-ray spectrum ($10^{22} < N_{\rm H} < 10^{23}\,{\rm cm^{-2}}$) but with broad lines in the optical spectrum and Intermediate/Type 1 characteristics in the SED (see Merloni et al. 2014). The final classification is performed according to the optical spectroscopic diagnostic, which divides the sample in almost an equal number of type 1 (22) and type 2 AGN (17).

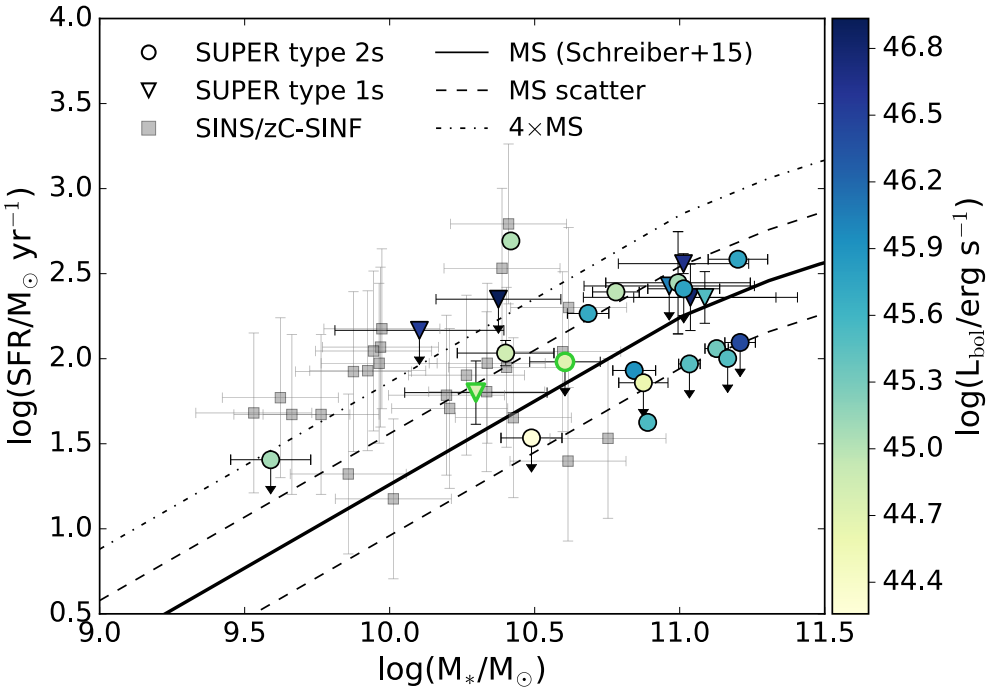

Fig. 5. Distribution of host galaxy properties in the SFR-M_* plane for the 24 AGN (type 1s marked by triangles and type 2s marked by circles) with star formation constraints in our sample as given in Table A.2. The two data points with green edges represent the targets with SFR derived through modeling of the stellar emission with SED fitting. The color coding indicates the AGN bolometric luminosity for each object of this subsample. The black solid line reproduces the main sequence (MS) of star-forming galaxies from Schreiber et al. (2015) at the average redshift of our target sample (i.e. ∼2.3). The dashed lines mark the scatter of the main sequence (equal to 0.3 dex) while the dot-dashed line represents the locus 4 times above the main sequence along the SFR axis (as defined by Rodighiero et al. 2011). The gray squares trace the properties of the 25 star-forming galaxies targeted by the SINS/zC-SINF survey (Förster Schreiber et al. 2018) without AGN signatures. We note that their selection based on a minimum SFR or Hα flux results in a preferentially higher sSFRs than the overall population of normal galaxies at those redshifts (see discussion in Förster Schreiber et al. 2009; Mancini et al. 2011). These galaxies, with IFS data comparable to the SUPER ones, will be our non-AGN comparison sample in future analyses (see text for more details).

4.3. Radio regime

All our AGN are located in fields targeted by radio surveys. In particular, the E-CDF-S has been observed with the Very Large Array (VLA) at 1.4 GHz (Miller et al. 2013), with a typical rms of 7.4 μJy beam^{-1} (2.8″ × 1.6″ beam size). A catalog of optical and IR counterparts for this survey is provided by Bonzini et al. (2012). As for the COSMOS field, we took advantage of the deep 3 GHz VLA-COSMOS project (Smolčić et al. 2017), characterized by an average rms sensitivity of 2.3 μJy beam^{-1} and an angular resolution of 0.75″. The other targets (from XMM-XXL, Stripe 82X and WISSH) are part of the VLA's FIRST survey at 1.4 GHz (Becker et al. 1995), with a typical 5σ sensitivity of 0.15 mJy beam^{-1} and a resolution of 5″.

We want to study the radio properties of our targets to see, in particular, which ones are jetted and non-jetted[8]. We do this by comparing their FIR and radio luminosities. Namely, when an object lies along the FIR-radio correlation both its radio and FIR emission are supposed to be driven by recent star-formation (Yun et al. 2001). Instead, if an object is off the correlation its "radio excess" is interpreted as evidence for radio emission from strong jets (Padovani 2017). In Fig. 7 (left panel) we plot these quantities for the 24 targets with detections or upper limits in the FIR regime for which we could derive FIR luminosities through SED-fitting modeling (Sect. 3.2). The values are reported in Table A.2. We computed the radio power at 1.4 GHz for all sources, converting the 3 GHz flux for the COSMOS targets assuming a radio spectral index $\alpha_r = 0.7$. For the objects without radio detections (blue hexagons in the left panel of Fig. 7) we used the 5σ sensitivity flux values (0.02, 0.037 and 0.15 mJy beam^{-1} for the COSMOS, CDF-S and XMM-XXL/Stripe82X/WISSH targets respectively) to estimate upper limits for the radio power. The plot includes ∼62% of the sample although most of the datapoints are actually radio and/or FIR upper limits. The comparison with the FIR-radio correlation and its 2σ dispersion shows the presence of 4 outliers: cid_451, cid_346, cid_1143 and XID36.

Since FIR luminosities are not available for the whole AGN sample, we further explored its radio properties by deriving the so-called q parameter, defined as the logarithm of the ratio between IR monochromatic and radio flux densities. The photometric band at the longest wavelength which allows us to use actual detections for most of the sample by keeping the number of upper limits as low as possible, is 24 μm. We therefore use $q_{24\,\mathrm{obs}} = \log(S_{24\,\mu\mathrm{m}}/S_r)$, where $S_{24\,\mu\mathrm{m}}$ is the observed flux density at 24 μm and S_r is that at 1.4 GHz (see, e.g., Bonzini et al. 2013). For the only target which is undetected at 24 μm and without an upper limit, S82X1940, we used an upper limit of 6 mJy given by the WISE All-sky survey 5σ sensitivity in the 22 μm *W4* filter. The distribution of $q_{24\,\mathrm{obs}}$ as a function of redshift is plotted in Fig. 7 (right panel). Red dots mark targets with detections both in the MIR and radio regime; blue-dot upper and lower limits represent sources with detections only in the radio or in the MIR, respectively; green squares depict AGN with upper limits both in the MIR and in the radio, for which the

[8] We follow Padovani (2017) and use this new nomenclature, which supersedes the old "radio-loud/radio-quiet" distinction.

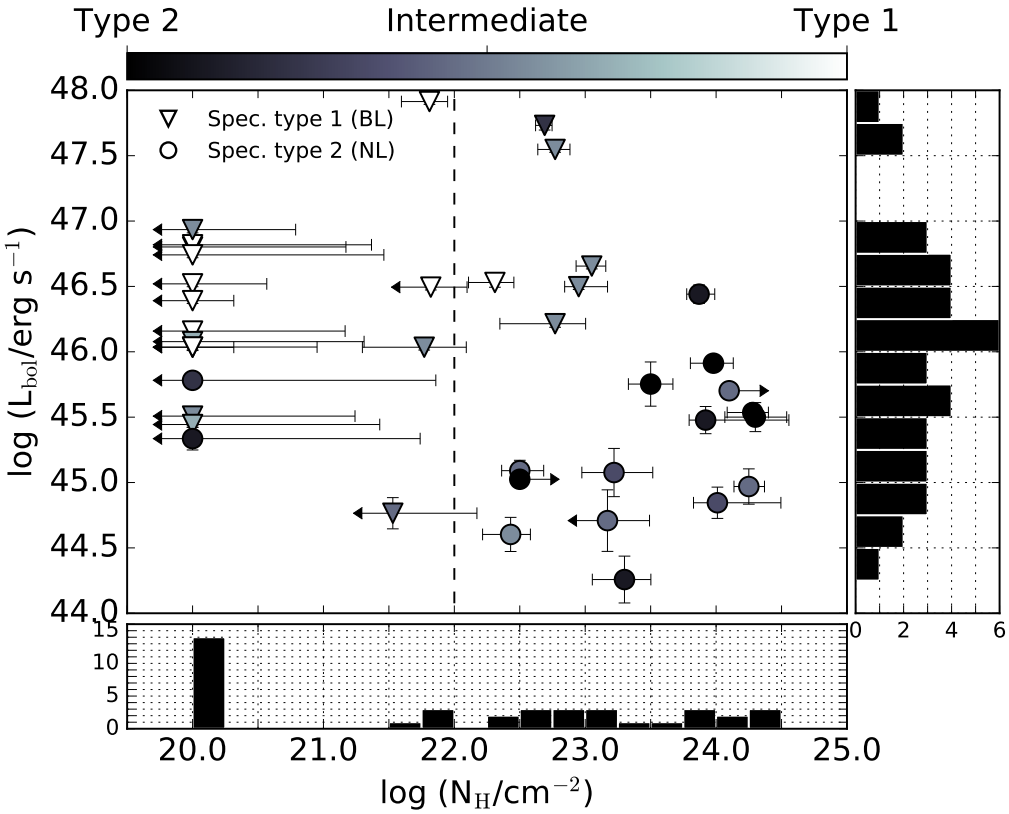

Fig. 6. AGN bolometric luminosities versus column densities of the whole target sample. These quantities are derived through SED-fitting modeling and X-ray spectral analysis, respectively. The dashed line at $\log(N_{\rm H}/{\rm cm}^{-2}) = 22$ marks the assumed separation between X-ray unobscured and obscured AGN. The black histograms show the projected distribution of the two quantities along each axis. The gray color scale depicts the inclination of the observer's line of sight with respect to the dusty torus equatorial plane derived from the SED-fitting analysis, which corresponds to type 2 for dark colors, type 1 for light colors and intermediate (i.e., the transition between the two classes of AGN) in between. The AGN type as derived from the optical spectra is depicted by the different symbols, triangles for type 1s and circles for type 2s. The comparison of the color coding and the different symbols to the location of the targets in the $L_{\rm bol} - N_{\rm H}$ plane suggests an agreement between the three classification methods and provides extra confidence in the SED-fitting results. The sample results to be almost equally divided in type 1 and type 2 AGN.

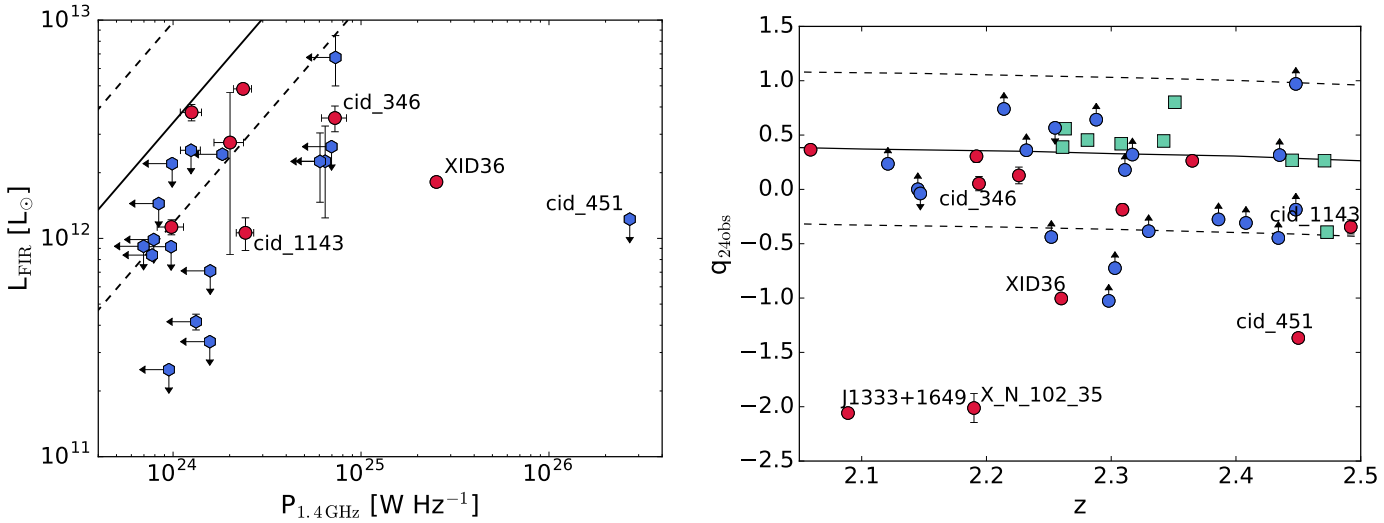

Fig. 7. Radio properties of the target sample. *Left panel*: FIR luminosities due to star formation versus radio power at 1.4 GHz. The solid line shows the Kennicutt (1998a) relation, given by $\log P_{1.4\,{\rm GHz}} = \log L_{\rm FIR} + 11.47$, while the dashed lines represent its 2σ dispersion. Red circles depict targets with radio detections, while blue hexagons mark targets with upper limits in the radio regime and/or in the FIR. The four AGN outside the 2σ dispersion and classified as jetted are marked by their ID. *Right panel*: $q_{24\,{\rm obs}} = \log(S_{24\,\mu{\rm m}}/S_{\rm r})$ plotted as a function of redshift for the whole AGN sample. Red dots mark targets with detections both in the MIR and radio regime; blue-dot upper and lower limits represent sources with detections only in the radio or in the MIR, respectively; green squares depict AGN with upper limits both in the MIR and in the radio. The solid line displays $q_{24\,{\rm obs}}$ versus redshift for M82 (from Bonzini et al. 2013), while dashed lines mark the $\pm 2\sigma$ dispersion. The six AGN classified as jetted, either from this plot of from the left panel of the figure, are marked by their ID.

two limits go in opposite directions. As done by Bonzini et al. (2013), we compare our results to the $q_{24\,\mathrm{obs}}$ of M82 (as representative of star-forming galaxies) and compute $q_{24\,\mathrm{obs}}$ from its SED as a function of redshift (for more details see Sect. 3.1.1 and Fig. 2 in Bonzini et al. 2013). The locus of star-forming galaxies is defined as the region of $\pm2\sigma$ around the M82 template (dashed lines in the plot) and sources below this region show a radio excess. We are fully aware of the fact that, using the 24 μm flux density (which corresponds to $\lambda \sim 7.3\,\mu$m rest-frame at the average z of the sample), we are actually probing a wavelength regime where the AGN can dominate the total energy budget. To have an estimate of the increase in $q_{24\,\mathrm{obs}}$ the AGN emission may produce, we evaluate the average AGN contribution to the total 24 μm flux from the SEDs where we can model all the emission components (i.e., 24 targets, 62% of the sample). The median value of this fraction is ∼86% which, when subtracted from $q_{24\,\mathrm{obs}}$, would produce a down shift of the data points by ∼0.8 dex. In the right panel of Fig. 7 the datapoints are already downshifted by such value. After accounting for this correction we find that four of our targets display a clear radio excess: the COSMOS target cid_451, whose jetted nature is confirmed also from the FIR-radio comparison; the CDF-S target XID36, which was inside the 2σ area before the correction but an outlier in the FIR-radio plane; the targets J1333+1649 and X_N_102_35, not plotted in the left panel of Fig. 7 because they lack an FIR detection. The targets cid_346 and cid_1143 are still within the dispersion after the correction, but classified as jetted according to the position in the FIR-radio plane. Combining the results of the two panels in Fig. 7, we estimate a jetted AGN fraction of 10−15%, which is consistent with the typical values observed in X-ray selected samples.

5. Summary and future work

We have presented the sample targeted by SUPER, an on-going ESO's VLT/SINFONI Large Programme assisted by AO facilities, designed to map the ionized gas kinematics down to ∼2 kpc spatial resolution in a representative sample of 39 AGN at $2 < z < 2.5$. It will provide a systematic investigation of AGN ionized outflows and their effects on star formation in the host galaxies, by exploring a wide range in AGN and host galaxies properties. The sample was selected in an unbiased way with respect to the chance of detecting outflows, with the aim to cover the widest possible range in AGN properties. In this first paper we fully characterized the physical properties of the AGN sample, drawn from X-ray surveys (i.e., CDF-S, COSMOS, XMM-XXL, Stripe82X, WISSH) which benefit from a wealth of multi-wavelength data, from the radio to the X-rays as follows:

- By collecting UV to FIR photometric data we built up the AGN SEDs and performed a detailed SED-fitting modeling which allowed us to derive stellar masses, $\log(M_*/M_\odot) = [9.6-11.2]$, SFR = [25−680] $M_\odot\,\mathrm{yr}^{-1}$, and AGN bolometric luminosities, $\log(L_{\mathrm{bol}}/\mathrm{erg\,s}^{-1}) = [44.3-47.9]$.
- A detailed X-ray spectral fitting was performed to determine column densities N_{H} up to 2×10^{24} cm^{-2} and X-ray 2−10 keV luminosities, $\log(L_{\mathrm{X}}/\mathrm{erg\,s}^{-1}) = [43.2-45.8]$.
- For AGN characterized by broad lines in their optical spectra we reported BH masses obtained using the "virial method" on the C IV and Hβ lines, with results in the range $\log(M_{\mathrm{BH}}/M_\odot) = [7.9-10.2]$. These values were combined with the bolometric luminosity to compute Eddington ratios for this subsample of AGN which includes BHs accreting at the Eddington limit and down to 10^{-2} times λ_{Edd}.
- Finally, we retrieved the radio fluxes (or upper limits) for each target and, by comparing their FIR luminosities (when available) or their 24 μm fluxes, we inferred the presence of at least 6 jetted AGN in our sample.

As clear from the wide parameter ranges given above, our survey probes a representative sample of AGN, in terms of both host galaxy properties, such as stellar mass and SFR, and AGN ones, like column density, AGN bolometric luminosity, BH mass and Eddington ratio. This will give us the context to place our IFS studies and the opportunity to investigate possible links among all these quantities and connect them to the outflow properties.

To achieve one of the main goals of the survey, namely inferring the impact that outflows may have on the ability of the host galaxy to form stars, we need to quantify their gas content. Molecular gas represents indeed the principal fuel for star formation in galaxies and the fundamental link between SF and AGN activity. In AGN host galaxies, molecular gas fractions ($f_{\mathrm{gas}} = M_{\mathrm{gas}}/M_*$) and depletion timescales ($t_{\mathrm{dep}} = M_{\mathrm{gas}}/\mathrm{SFR}$) appear to be smaller than the values measured for the parent population of star-forming galaxies (e.g., Kakkad et al. 2017; Brusa et al. 2018, but see also Husemann et al. 2017a; Rosario et al. 2018). The interpretation of these quantities is non-trivial and requires a joint characterization of the cold molecular and ionized gas phase. SUPER will achieve this goal by combining the SINFONI observations with two on-going programs with ALMA and APEX:

- SUPER-ALMA (PI: Mainieri; Circosta et al., in prep.), which has been allocated 12.6 and 19.5 h of ALMA Band-3 observing time in Cycle 4 and 5 respectively, to target the CO(3-2) emission line with 1″ angular resolution over a sample constructed to include the SUPER sources. This project will perform a systematic study of the gas content of AGN hosts, in order to derive gas fractions and depletion timescales, but will also complement the goals of our SINFONI survey. In fact, information about the possible presence of outflows in these targets will be available and will allow us to infer whether there is a causal connection between a lower gas fraction and the presence of an AGN-driven outflow.
- SUPER-APEX (PI: Cicone), a pilot project with the APEX PI230 Rx receiver that was allocated 28.2 h to observe, in two of our targets, the [C I](2-1) transition as a tracer of the total amount of cold H_2 and the CO(7-6) transition, which will trace the warmer and denser phase of H_2.

Recent studies showed that a significant fraction of the mass and momentum of AGN-driven outflows can be contained in the molecular gas phase (e.g., Cicone et al. 2014; Carniani et al. 2015; Fiore et al. 2017). To obtain a comprehensive picture of the feedback processes, it is crucial to investigate the molecular gas properties. The next step will be to map the molecular gas, tracing the fuel for star formation and feedback, with the same ∼kpc spatial resolution of the ionized gas (e.g., Cicone et al. 2018). A comprehensive and dynamic view of the evolution of the star formation process and the impact of AGN feedback across the host galaxy, at the peak epoch of galaxy assembly, will be finally possible. This will have far reaching implications on theoretical models and simulations of galaxy-AGN evolution. The final goal of the SUPER project is to be a reference legacy survey for future work and to establish a unique statistical sample at high redshift characterized by a wide set of ancillary data. The systematic approach adopted will reveal key clues about outflow physics and feedback in AGN host galaxies.

Acknowledgements. We thank the anonymous referee for carefully reading the paper and providing comments. C. Circosta also thanks: D. Burgarella and L. Ciesla for helpful advice in using Cigale; I. Baronchelli, G. Calistro Rivera, A. Feltre, E. Hatziminaoglou and D. Rosario for useful discussions about SED fitting; E. Le Floc'h for providing MIPS fluxes for the targets cid_971 and lid_206; Y.-Y. Chang and I. Delvecchio for providing their SED-fitting results, and F. Duras for the WISSH photometric catalog; E. Lusso for providing the data of her sample plotted in Fig. 3 and P. Lang, D. Liu and J. Scholtz for the ALMA data of COSMOS and CDF-S; A. Zanella for helpful discussions and support while the paper was written. C. Circosta acknowledges support from the IMPRS on Astrophysics at the LMU (Munich). CF and CC acknowledge support from the European Union Horizon 2020 research and innovation programme under the Marie Sklodowska-Curie grant agreement No 664931. BM acknowledges support by the Collaborative Research Centre 956, sub-project A1, funded by the Deutsche Forschungsgemeinschaft (DFG). GC acknowledges the support by INAF/Frontiera through the "Progetti Premiali" funding scheme of the Italian Ministry of Education, University, and Research. GC has been supported by the INAF PRIN-SKA 2017 programme 1.05.01.88.04. This research project was supported by the DFG Cluster of Excellence "Origin and Structure of the Universe" (http://www.universe-cluster.de/). This research has made use of the following data: data based on data products from observations made with ESO Telescopes at the La Silla Paranal Observatory under ESO programme ID 179.A-2005 and on data products produced by TERAPIX and the Cambridge Astronomy Survey Unit on behalf of the UltraVISTA consortium. Data from HerMES project (http://sro.sussex.ac.uk/40970/). HerMES is a Herschel Key Programme utilising Guaranteed Time from the SPIRE instrument team, ESAC scientists and a mission scientist. The HerMES data was accessed through the Herschel Database in Marseille (HeDaM – http://hedam.lam.fr) operated by CeSAM and hosted by the Laboratoire d'Astrophysique de Marseille. HerMES DR3 was made possible through support of the Herschel Extragalactic Legacy Project, HELP (http://herschel.sussex.ac.uk), HELP is a European Commission Research Executive Agency funded project under the SP1-Cooperation, Collaborative project, Small or medium-scale focused research project, FP7-SPACE-2013-1 scheme.

References

Aird, J., Coil, A. L., Moustakas, J., et al. 2012, ApJ, 746, 90
Alexander, D. M., Swinbank, A. M., Smail, I., McDermid, R., & Nesvadba, N. P. H. 2010, MNRAS, 402, 2211
Ananna, T. T., Salvato, M., LaMassa, S., et al. 2017, ApJ, 850, 66
Arnaud, K. A. 1996, in Astronomical Data Analysis Software and Systems V, eds. G. H. Jacoby, & J. Barnes, ASP Conf. Ser., 101, 17
Bae, H.-J., Woo, J.-H., Karouzos, M., et al. 2017, ApJ, 837, 91
Balestra, I., Mainieri, V., Popesso, P., et al. 2010, A&A, 512, A12
Becker, R. H., White, R. L., & Helfand, D. J. 1995, ApJ, 450, 559
Behroozi, P. S., Wechsler, R. H., & Conroy, C. 2013, ApJ, 770, 57
Bischetti, M., Piconcelli, E., Vietri, G., et al. 2017, A&A, 598, A122
Bongiorno, A., Merloni, A., Brusa, M., et al. 2012, MNRAS, 427, 3103
Bonzini, M., Mainieri, V., Padovani, P., et al. 2012, ApJS, 203, 15
Bonzini, M., Padovani, P., Mainieri, V., et al. 2013, MNRAS, 436, 3759
Boquien, M., Kennicutt, R., Calzetti, D., et al. 2016, A&A, 591, A6
Brandt, W. N., & Alexander, D. M. 2015, A&A Rev., 23, 1
Brusa, M., Bongiorno, A., Cresci, G., et al. 2015, MNRAS, 446, 2394
Brusa, M., Perna, M., Cresci, G., et al. 2016, A&A, 588, A58
Brusa, M., Cresci, G., Daddi, E., et al. 2018, A&A, 612, A29
Bruzual, G., & Charlot, S. 2003, MNRAS, 344, 1000
Buat, V., Giovannoli, E., Heinis, S., et al. 2011, A&A, 533, A93
Buat, V., Noll, S., Burgarella, D., et al. 2012, A&A, 545, A141
Buat, V., Oi, N., Heinis, S., et al. 2015, A&A, 577, A141
Calzetti, D., Armus, L., Bohlin, R. C., et al. 2000, ApJ, 533, 682
Cano-Díaz, M., Maiolino, R., Marconi, A., et al. 2012, A&A, 537, L8
Capak, P., Aussel, H., Ajiki, M., et al. 2007, ApJS, 172, 99
Cardamone, C. N., van Dokkum, P. G., Urry, C. M., et al. 2010, ApJS, 189, 270
Carniani, S., Marconi, A., Maiolino, R., et al. 2015, A&A, 580, A102
Carniani, S., Marconi, A., Maiolino, R., et al. 2016, A&A, 591, A28
Cash, W. 1979, ApJ, 228, 939
Chabrier, G. 2003, PASP, 115, 763
Chang, Y.-Y., Le Floc'h, E., Juneau, S., et al. 2017, ApJS, 233, 19
Charlot, S., & Fall, S. M. 2000, ApJ, 539, 718
Cicone, C., Maiolino, R., Sturm, E., et al. 2014, A&A, 562, A21
Cicone, C., Maiolino, R., Gallerani, S., et al. 2015, A&A, 574, A14
Cicone, C., Brusa, M., Ramos Almeida, C., et al. 2018, Nat. Astron., 2, 176
Ciesla, L., Charmandaris, V., Georgakakis, A., et al. 2015, A&A, 576, A10
Ciotti, L., & Ostriker, J. P. 1997, ApJ, 487, L105
Civano, F., Marchesi, S., Comastri, A., et al. 2016, ApJ, 819, 62
Concas, A., Popesso, P., Brusa, M., et al. 2017, A&A, 606, A36
Costa, T., Sijacki, D., & Haehnelt, M. G. 2014, MNRAS, 444, 2355
Crenshaw, D. M., & Kraemer, S. B. 2007, ApJ, 659, 250
Cresci, G., & Maiolino, R. 2018, Nat. Astron., 2, 179
Cresci, G., Hicks, E. K. S., Genzel, R., et al. 2009, ApJ, 697, 115
Cresci, G., Mainieri, V., Brusa, M., et al. 2015, ApJ, 799, 82
Cullen, F., McLure, R. J., Khochfar, S., et al. 2018, MNRAS
Dale, D. A., Helou, G., Magdis, G. E., et al. 2014, ApJ, 784, 83
Das, V., Crenshaw, D. M., Hutchings, J. B., et al. 2005, AJ, 130, 945
Debuhr, J., Quataert, E., & Ma, C.-P. 2012, MNRAS, 420, 2221
Delvecchio, I., Smolčić, V., Zamorani, G., et al. 2017, A&A, 602, A3
Di Matteo, T., Springel, V., & Hernquist, L. 2005, Nature, 433, 604
Duras, F., Bongiorno, A., Piconcelli, E., et al. 2017, A&A, 604, A67
Elbaz, D., Dickinson, M., Hwang, H. S., et al. 2011, A&A, 533, A119
Erben, T., Hildebrandt, H., Miller, L., et al. 2013, MNRAS, 433, 2545
Fabian, A. C. 2012, ARA&A, 50, 455
Feltre, A., Hatziminaoglou, E., Fritz, J., & Franceschini, A. 2012, MNRAS, 426, 120
Feruglio, C., Maiolino, R., Piconcelli, E., et al. 2010, A&A, 518, L155
Fiore, F., Feruglio, C., Shankar, F., et al. 2017, A&A, 601, A143
Fliri, J., & Trujillo, I. 2016, MNRAS, 456, 1359
Förster Schreiber, N. M., Genzel, R., Bouché, N., et al. 2009, ApJ, 706, 1364
Förster Schreiber, N. M., Genzel, R., Newman, S. F., et al. 2014, ApJ, 787, 38
Förster Schreiber, N. M., Renzini, A., Mancini, C., et al. 2018, ApJS, 238, 21
Fotopoulou, S., Pacaud, F., Paltani, S., et al. 2016, A&A, 592, A5
Fritz, J., Franceschini, A., & Hatziminaoglou, E. 2006, MNRAS, 366, 767
Georgakakis, A., Salvato, M., Liu, Z., et al. 2017, MNRAS, 469, 3232
Gnerucci, A., Marconi, A., Cresci, G., et al. 2011, A&A, 528, A88
Guo, Y., Ferguson, H. C., Giavalisco, M., et al. 2013, ApJS, 207, 24
Harrison, C. M. 2017, Nat. Astron., 1, 0165
Harrison, C. M., Alexander, D. M., Swinbank, A. M., et al. 2012, MNRAS, 426, 1073
Harrison, C. M., Alexander, D. M., Mullaney, J. R., & Swinbank, A. M. 2014, MNRAS, 441, 3306
Harrison, C. M., Alexander, D. M., Mullaney, J. R., et al. 2016, MNRAS, 456, 1195
Harrison, C. M., Costa, T., Tadhunter, C. N., et al. 2018, Nat. Astron., 2, 198
Hatziminaoglou, E., Fritz, J., Franceschini, A., et al. 2008, MNRAS, 386, 1252
Häussler, B., McIntosh, D. H., Barden, M., et al. 2007, ApJS, 172, 615
Heckman, T. M., Kauffmann, G., Brinchmann, J., et al. 2004, ApJ, 613, 109
Hinshaw, G., Larson, D., Komatsu, E., et al. 2013, ApJS, 208, 19
Hsieh, B.-C., Wang, W.-H., Hsieh, C.-C., et al. 2012, ApJS, 203, 23
Hsu, L.-T., Salvato, M., Nandra, K., et al. 2014, ApJ, 796, 60
Hurley, P. D., Oliver, S., Betancourt, M., et al. 2017, MNRAS, 464, 885
Husemann, B., Wisotzki, L., Sánchez, S. F., & Jahnke, K. 2013, A&A, 549, A43
Husemann, B., Jahnke, K., Sánchez, S. F., et al. 2014, MNRAS, 443, 755
Husemann, B., Davis, T. A., Jahnke, K., et al. 2017a, MNRAS, 470, 1570
Husemann, B., Tremblay, G., Davis, T., et al. 2017b, The Messenger, 169, 42
Ilbert, O., Capak, P., Salvato, M., et al. 2009, ApJ, 690, 1236
Ilbert, O., McCracken, H. J., Le Fèvre, O., et al. 2013, A&A, 556, A55
Inoue, A. K. 2011, MNRAS, 415, 2920
Jaffe, W., Meisenheimer, K., Röttgering, H. J. A., et al. 2004, Nature, 429, 47
Kakkad, D., Mainieri, V., Padovani, P., et al. 2016, A&A, 592, A148
Kakkad, D., Mainieri, V., Brusa, M., et al. 2017, MNRAS, 468, 4205
Karouzos, M., Woo, J.-H., & Bae, H.-J. 2016, ApJ, 819, 148
Kennicutt, R. C., Jr. 1998a, ARA&A, 36, 189
Kennicutt, R. C., Jr. 1998b, ApJ, 498, 541
King, A. 2005, ApJ, 635, L121
King, A., & Pounds, K. 2015, ARA&A, 53, 115
Kormendy, J., & Ho, L. C. 2013, ARA&A, 51, 511
Kurk, J., Cimatti, A., Daddi, E., et al. 2013, A&A, 549, A63
Laigle, C., McCracken, H. J., Ilbert, O., et al. 2016, ApJS, 224, 24
LaMassa, S. M., Urry, C. M., Cappelluti, N., et al. 2016, ApJ, 817, 172
Lang, D., Hogg, D. W., & Schlegel, D. J. 2016, AJ, 151, 36
Lani, C., Netzer, H., & Lutz, D. 2017, MNRAS, 471, 59
Lanzuisi, G., Piconcelli, E., Fiore, F., et al. 2009, A&A, 498, 67
Lanzuisi, G., Civano, F., Elvis, M., et al. 2013, MNRAS, 431, 978
Lanzuisi, G., Civano, F., Marchesi, S., et al. 2018, MNRAS, 480, 2578
Lehmer, B. D., Brandt, W. N., Alexander, D. M., et al. 2005, ApJS, 161, 21
Liu, G., Zakamska, N. L., Greene, J. E., Nesvadba, N. P. H., & Liu, X. 2013, MNRAS, 430, 2327
Liu, G., Zakamska, N. L., & Greene, J. E. 2014, MNRAS, 442, 1303
Liu, G., Arav, N., & Rupke, D. S. N. 2015, ApJS, 221, 9
Liu, Z., Merloni, A., Georgakakis, A., et al. 2016, MNRAS, 459, 1602
Lo Faro, B., Buat, V., Roehlly, Y., et al. 2017, MNRAS, 472, 1372
Luo, B., Brandt, W. N., Xue, Y. Q., et al. 2017, ApJS, 228, 2
Lusso, E., & Risaliti, G. 2016, ApJ, 819, 154
Lusso, E., Comastri, A., Simmons, B. D., et al. 2012, MNRAS, 425, 623
Lutz, D., Poglitsch, A., Altieri, B., et al. 2011, A&A, 532, A90

Madau, P., & Dickinson, M. 2014, ARA&A, 52, 415
Magnelli, B., Popesso, P., Berta, S., et al. 2013, A&A, 553, A132
Mainieri, V., Bergeron, J., Hasinger, G., et al. 2002, A&A, 393, 425
Mainieri, V., Bongiorno, A., Merloni, A., et al. 2011, A&A, 535, A80
Mancini, C., Förster Schreiber, N. M., Renzini, A., et al. 2011, ApJ, 743, 86
Marchesi, S., Civano, F., Elvis, M., et al. 2016a, ApJ, 817, 34
Marchesi, S., Lanzuisi, G., Civano, F., et al. 2016b, ApJ, 830, 100
Martocchia, S., Piconcelli, E., Zappacosta, L., et al. 2017, A&A, 608, A51
Menzel, M.-L., Merloni, A., Georgakakis, A., et al. 2016, MNRAS, 457, 110
Merloni, A., Bongiorno, A., Brusa, M., et al. 2014, MNRAS, 437, 3550
Miller, N. A., Bonzini, M., Fomalont, E. B., et al. 2013, ApJS, 205, 13
Molnár, D. C., Sargent, M. T., Elbaz, D., Papadopoulos, P. P., & Silk, J. 2017, MNRAS, 467, 586
Mor, R., & Netzer, H. 2012, MNRAS, 420, 526
Mullaney, J. R., Alexander, D. M., Goulding, A. D., & Hickox, R. C. 2011, MNRAS, 414, 1082
Murphy, K. D., & Yaqoob, T. 2009, MNRAS, 397, 1549
Nenkova, M., Sirocky, M. M., Ivezić, Ž., & Elitzur, M. 2008, ApJ, 685, 147
Nesvadba, N. P. H., Lehnert, M. D., Eisenhauer, F., et al. 2006, ApJ, 650, 693
Nesvadba, N. P. H., Lehnert, M. D., De Breuck, C., Gilbert, A., & van Breugel, W. 2007, A&A, 475, 145
Nesvadba, N. P. H., Lehnert, M. D., De Breuck, C., Gilbert, A. M., & van Breugel, W. 2008, A&A, 491, 407
Nesvadba, N. P. H., Polletta, M., Lehnert, M. D., et al. 2011, MNRAS, 415, 2359
Nesvadba, N. P. H., De Breuck, C., Lehnert, M. D., Best, P. N., & Collet, C. 2017a, A&A, 599, A123
Nesvadba, N. P. H., Drouart, G., De Breuck, C., et al. 2017b, A&A, 600, A121
Noeske, K. G., Weiner, B. J., Faber, S. M., et al. 2007, ApJ, 660, L43
Noll, S., Burgarella, D., Giovannoli, E., et al. 2009, A&A, 507, 1793
Oliver, S. J., Bock, J., Altieri, B., et al. 2012, MNRAS, 424, 1614
Padovani, P. 2017, Nat. Astron., 1, 0194
Padovani, P., Alexander, D. M., Assef, R. J., et al. 2017, A&ARv, 25, 2
Perna, M., Brusa, M., Salvato, M., et al. 2015, A&A, 583, A72
Perna, M., Lanzuisi, G., Brusa, M., Mignoli, M., & Cresci, G. 2017, A&A, 603, A99
Piconcelli, E., Jimenez-Bailón, E., Guainazzi, M., et al. 2005, A&A, 432, 15
Pierre, M., Pacaud, F., Adami, C., et al. 2016, A&A, 592, A1
Polletta, M., Tajer, M., Maraschi, L., et al. 2007, ApJ, 663, 81
Prieto, M. A., Reunanen, J., Tristram, K. R. W., et al. 2010, MNRAS, 402, 724
Puglisi, A., Rodighiero, G., Franceschini, A., et al. 2016, A&A, 586, A83
Reddy, N. A., Kriek, M., Shapley, A. E., et al. 2015, ApJ, 806, 259
Richards, G. T., Lacy, M., Storrie-Lombardi, L. J., et al. 2006, ApJS, 166, 470
Rodighiero, G., Daddi, E., Baronchelli, I., et al. 2011, ApJ, 739, L40
Rosario, D. J., Burtscher, L., Davies, R. I., et al. 2018, MNRAS, 473, 5658
Roseboom, I. G., Oliver, S. J., Kunz, M., et al. 2010, MNRAS, 409, 48
Roseboom, I. G., Ivison, R. J., Greve, T. R., et al. 2012, MNRAS, 419, 2758
Rupke, D. S. N., & Veilleux, S. 2013, ApJ, 775, L15
Rupke, D. S. N., Gültekin, K., & Veilleux, S. 2017, ApJ, 850, 40
Salvato, M., Hasinger, G., Ilbert, O., et al. 2009, ApJ, 690, 1250
Santini, P., Ferguson, H. C., Fontana, A., et al. 2015, ApJ, 801, 97
Sarazin, M., Melnick, J., Navarrete, J., & Lombardi, G. 2008, The Messenger, 132, 11
Schinnerer, E., Smolčić, V., Carilli, C. L., et al. 2007, ApJS, 172, 46
Schlegel, D. J., Finkbeiner, D. P., & Davis, M. 1998, ApJ, 500, 525
Scholtz, J., Alexander, D. M., Harrison, C. M., et al. 2018, MNRAS, 475, 1288
Schreiber, C., Pannella, M., Elbaz, D., et al. 2015, A&A, 575, A74
Shen, Y., Greene, J. E., Ho, L. C., et al. 2015, ApJ, 805, 96
Silk, J., & Rees, M. J. 1998, A&A, 331, L1
Simm, T., Salvato, M., Saglia, R., et al. 2016, A&A, 585, A129
Smolčić, V., Novak, M., Bondi, M., et al. 2017, A&A, 602, A1
Somerville, R. S., Hopkins, P. F., Cox, T. J., Robertson, B. E., & Hernquist, L. 2008, MNRAS, 391, 481
Springel, V., Di Matteo, T., & Hernquist, L. 2005, MNRAS, 361, 776
Stalevski, M., Fritz, J., Baes, M., Nakos, T., & Popović, L. Č. 2012, MNRAS, 420, 2756
Stalevski, M., Ricci, C., Ueda, Y., et al. 2016, MNRAS, 458, 2288
Stevans, M. L., Shull, J. M., Danforth, C. W., & Tilton, E. M. 2014, ApJ, 794, 75
Strateva, I., Ivezić, Ž., Knapp, G. R., et al. 2001, AJ, 122, 1861
Suh, H., Civano, F., Hasinger, G., et al. 2017, ApJ, 841, 102
Symeonidis, M., Giblin, B. M., Page, M. J., et al. 2016, MNRAS, 459, 257
Szokoly, G. P., Bergeron, J., Hasinger, G., et al. 2004, ApJS, 155, 271
Telfer, R. C., Zheng, W., Kriss, G. A., & Davidsen, A. F. 2002, ApJ, 565, 773
Tombesi, F., Sambruna, R. M., Reeves, J. N., et al. 2010, ApJ, 719, 700
Tombesi, F., Meléndez, M., Veilleux, S., et al. 2015, Nature, 519, 436
Trakhtenbrot, B., & Netzer, H. 2012, MNRAS, 427, 3081
Vayner, A., Wright, S. A., Murray, N., et al. 2017, ApJ, 851, 126
Veilleux, S., Bolatto, A., Tombesi, F., et al. 2017, ApJ, 843, 18
Vestergaard, M., & Peterson, B. M. 2006, ApJ, 641, 689
Vietri, G., Piconcelli, E., Bischetti, M., et al. 2018, A&A, 617, A81
Vito, F., Vignali, C., Gilli, R., et al. 2013, MNRAS, 428, 354
Wachter, K., Leach, R., & Kellogg, E. 1979, ApJ, 230, 274
Weedman, D., Sargsyan, L., Lebouteiller, V., Houck, J., & Barry, D. 2012, ApJ, 761, 184
Woo, J.-H., Bae, H.-J., Son, D., & Karouzos, M. 2016, ApJ, 817, 108
Xue, Y. Q., Luo, B., Brandt, W. N., et al. 2016, ApJS, 224, 15
Yun, M. S., Reddy, N. A., & Condon, J. J. 2001, ApJ, 554, 803

[1] European Southern Observatory, Karl-Schwarzschild-Str. 2, 85748 Garching bei München, Germany
e-mail: ccircost@eso.org
[2] Ludwig Maximilian Universität, Professor-Huber-Platz 2, 80539 München, Germany
[3] Dipartimento di Fisica e Astronomia dell'Universitá degli Studi di Bologna, via P. Gobetti 93/2, 40129 Bologna, Italy
[4] INAF/OAS, Osservatorio di Astrofisica e Scienza dello Spazio di Bologna, via P. Gobetti 93/3, 40129 Bologna, Italy
[5] MPE, Giessenbach-Str. 1, 85748 Garching bei München, Germany
[6] Cluster of Excellence, Boltzmann-Str. 2, 85748 Garching bei München, Germany
[7] European Southern Observatory, Alonso de Cordova 3107, Casilla 19, 19001 Santiago, Chile
[8] CEA, IRFU, DAp, AIM, Université Paris-Saclay, Université Paris Diderot, Sorbonne Paris Cité, CNRS, 91191 Gif-sur-Yvette, France
[9] INAF – Osservatorio Astronomico di Padova, Vicolo dell'Osservatorio 5, 35122 Padova, Italy
[10] INAF – Osservatorio Astronomico di Brera, Via Brera 28, 20121 Milano, Italy
[11] Max-Planck-Institut für Astronomie, Königstuhl 17, 69117 Heidelberg, Germany
[12] INAF – Osservatorio Astronomico di Roma, Via Frascati 33, 00078 Monte Porzio Catone (Roma), Italy
[13] Universitá degli Studi di Roma "Tor Vergata", Via Orazio Raimondo 18, 00173 Roma, Italy
[14] Cavendish Laboratory, University of Cambridge, 19 J. J. Thomson Avenue, CB3 0HE Cambridge, UK
[15] Kavli Institute for Cosmology, University of Cambridge, Madingley Road, CB3 0HA Cambridge, UK
[16] Harvard-Smithsonian Center for Astrophysics, 60 Garden Street, 02138 Cambridge, MA, USA
[17] INAF – Osservatorio Astrofisico di Arcetri, Largo E. Fermi 5, 50125 Firenze, Italy
[18] INAF – Osservatorio Astronomico di Trieste, via G.B. Tiepolo 11, 34143 Trieste, Italy
[19] Centre for Extragalactic Astronomy, Department of Physics, Durham University, South Road, DH1 3LE Durham, UK
[20] Argelander-Institut für Astronomie, Universität Bonn, Auf dem Hügel 71, 53121 Bonn, Germany
[21] Space Science Data Center – ASI, via del Politecnico SNC, 00133 Roma, Italy
[22] Dipartimento di Fisica e Astronomia, Università di Firenze, Via G. Sansone 1, 50019 Sesto Fiorentino (Firenze), Italy
[23] School of Physics and Astronomy, Tel Aviv University, 69978 Tel Aviv, Israel
[24] Dipartimento di Fisica e Astronomia, Universitá di Padova, vicolo Osservatorio 3, 35122 Padova, Italy
[25] National Astronomical Observatory of Japan, Mitaka, 181-8588 Tokyo, Japan
[26] Kavli Institute for the Physics and Mathematics of the Universe, The University of Tokyo, 277-8583 Kashiwa, Japan

Appendix A: Properties of the target sample

Table A.1. Summary of the target AGN sample.

Field (1)	ID (2)	RA[J2000] (3)	Dec[J2000] (4)	z_{spec} (5)	H-band mag (6)	K-band mag (7)
XMM-XXL	X_N_160_22	02:04:53.81	−06:04:07.82	2.445	19.22	18.79
	X_N_81_44	02:17:30.95	−04:18:23.66	2.311	18.78	18.43
	X_N_53_3	02:20:29.84	−02:56:23.41	2.434	20.60	–
	X_N_66_23	02:22:33.64	−05:49:02.73	2.386	20.56	20.33
	X_N_35_20	02:24:02.71	−05:11:30.82	2.261	22.07	21.70
	X_N_12_26	02:25:50.09	−03:06:41.16	2.471	19.83	19.53
	X_N_44_64	02:27:01.46	−04:05:06.73	2.252	21.31	20.77
	X_N_4_48	02:27:44.63	−03:42:05.46	2.317	19.57	20.43
	X_N_102_35	02:29:05.94	−04:02:42.99	2.190	18.76	18.19
	X_N_115_23	02:30:05.66	−05:08:14.10	2.342	19.79	19.26
CDF-S	XID36	03:31:50.77	−27:47:03.41	2.259	21.49	20.80
	XID57[a]	03:31:54.40	−27:56:49.70	2.298	23.49	22.19
	XID419	03:32:23.44	−27:42:54.97	2.145	22.44	21.84
	XID427	03:32:24.20	−27:42:57.51	2.303	22.48	21.83
	XID522	03:32:28.50	−27:46:57.99	2.309	22.98	22.27
	XID614	03:32:33.02	−27:42:00.33	2.448	22.59	21.82
COSMOS	cid_166	09:58:58.68	+02:01:39.22	2.448	18.55	18.23
	lid_1289	09:59:14.65	+01:36:34.99	2.408	22.29	21.51
	cid_1057	09:59:15.00	+02:06:39.65	2.214	21.70	21.09
	cid_1605	09:59:19.82	+02:42:38.73	2.121	20.63	20.14
	cid_337	09:59:30.39	+02:06:56.08	2.226	22.12	21.54
	cid_346	09:59:43.41	+02:07:07.44	2.219	19.24	18.95
	cid_451	10:00:00.61	+02:15:31.06	2.450	21.88	21.37
	cid_1205	10:00:02.57	+02:19:58.68	2.255	21.64	20.72
	cid_2682	10:00:08.81	+02:06:37.66	2.435	21.46	21.17
	cid_1143	10:00:08.84	+02:15:27.99	2.492	22.90	22.27
	cid_467	10:00:24.48	+02:06:19.76	2.288	19.34	18.91
	cid_852	10:00:44.21	+02:02:06.76	2.232	21.53	21.05
	cid_971	10:00:59.45	+02:19:57.44	2.473	22.58	22.10
	cid_38	10:01:02.83	+02:03:16.63	2.192	20.42	20.21
	lid_206	10:01:15.56	+02:37:43.44	2.330	22.38	21.97
	cid_1253	10:01:30.57	+02:18:42.57	2.147	21.30	20.72
WISSH	J1333+1649	13:33:35.79	+16:49:03.96	2.089	15.72	15.49
	J1441+0454	14:41:05.54	+04:54:54.96	2.059	17.15	16.53
	J1549+1245	15:49:38.73	+12:45:09.20	2.365	15.92	15.34
Stripe82X	S82X1905	23:28:56.35	−00:30:11.74	2.263	19.72	19.15
	S82X1940	23:29:40.28	−00:17:51.68	2.351	20.80	20.15
	S82X2058	23:31:58.62	−00:54:10.44	2.308	19.79	19.29
	S82X2106	23:32:53.24	−00:33:35.35	2.281	20.56	20.23

Notes. (1) Field where the targets are located. (2) Source identification number from the catalogs corresponding to each field, i.e., Menzel et al. (2016), Luo et al. (2017), Civano et al. (2016), Martocchia et al. (2017) and LaMassa et al. (2016), respectively (see also Sect. 2.1). (3) RA and (4) Dec, given for the optical counterpart: the XMM-XXL targets have an SDSS counterpart whose coordinates are given in Menzel et al. (2016); for the targets in the CDF-S we report the CANDELS coordinates when available (we use the GEMS coordinates from Häussler et al. (2007) for the targets XID36 and XID57 since they are outside the CANDELS area), as given in Luo et al. (2017); for the COSMOS field we list the i-band coordinates taken from Marchesi et al. (2016a); the information for the WISSH subsample is available in Martocchia et al. (2017); for the targets in Stripe82X we give the SDSS coordinates from LaMassa et al. (2016). (5) Spectroscopic redshift, taken from the papers listed above. (6) H-band and (7) K-band AB magnitudes. [(a)] We took the redshift available in Xue et al. (2016), since Luo et al. (2017) provide a different redshift flagged as "Insecure".

Table A.2. Target sample properties summary, for both AGN and host galaxies.

ID	AGN type	$\log \frac{M_*}{M_\odot}$	$\log \frac{L_{\rm FIR}}{\rm erg\,s^{-1}}$	SFR ($M_\odot\,{\rm yr}^{-1}$)	$\log \frac{L_{\rm bol}}{\rm erg\,s^{-1}}$	X-ray net counts	$\log \frac{N_{\rm H}}{\rm cm^{-2}}$	$\log \frac{L_{[2-10\,{\rm keV}]}}{\rm erg\,s^{-1}}$	$\log \frac{M_{\rm BH}}{M_\odot}$	$\log \frac{P_{1.4\,{\rm GHz}}}{\rm W\,Hz^{-1}}$
(1)	(2)	(3)	(4)	(5)	(6)	(7)	(8)	(9)	(10)	(11)
X_N_160_22	BL	–	–	–	46.74 ± 0.02	24.5 ± 4.9	<22.32	$44.77^{+0.14}_{-0.19}$	8.9 ± 0.2	<24.87
X_N_81_44	BL	11.04 ± 0.37	45.93 ± 0.20	229 ± 103	46.80 ± 0.03	94.8 ± 9.7	<21.86	$44.77^{+0.07}_{-0.09}$	9.2 ± 0.1	<24.81
X_N_53_3	BL	–	46.41 ± 0.11	686 ± 178	46.21 ± 0.03	25.8 ± 5.1	$22.77^{+0.37}_{-0.67}$	$44.80^{+0.10}_{-0.13}$	8.7 ± 0.1	<24.86
X_N_66_23	BL	10.96 ± 0.29	<46.00	<268	46.04 ± 0.02	118.7 ± 10.9	<21.51	$44.71^{+0.06}_{-0.08}$	8.3 ± 0.2	<24.84
X_N_35_20	BL	–	–	–	45.44 ± 0.02	38.1 ± 6.2	<22.27	$44.00^{+0.07}_{-0.40}$	8.7 ± 0.1	<24.79
X_N_12_26	BL	–	–	–	46.52 ± 0.02	61.3 ± 7.8	<20.90	$44.56^{+0.13}_{-0.12}$	8.9 ± 0.1	<24.88
X_N_44_64	BL	11.09 ± 0.25	45.93 ± 0.15	229 ± 80	45.51 ± 0.07	51.8 ± 7.2	<21.97	$44.21^{+0.11}_{-0.17}$	9.1 ± 0.2	<24.78
X_N_4_48	BL	–	–	–	46.16 ± 0.02	58.2 ± 7.6	<21.85	$44.52^{+0.09}_{-0.16}$	9.1 ± 0.2	<24.81
X_N_102_35[a]	BL	–	–	–	46.82 ± 0.02	79.0 ± 8.9	<22.17	$45.37^{+0.05}_{-0.11}$	8.9 ± 0.1	27.05 ± 0.01
X_N_115_23	BL	–	–	–	46.49 ± 0.02	131.8 ± 11.5	<22.26	$44.93^{+0.08}_{-0.10}$	8.4 ± 0.1	<24.82
XID36[a]	NL	10.68 ± 0.07	45.84 ± 0.02	184 ± 9	45.70 ± 0.06	47.2 ± 6.9	[b]>24.1	$43.84^{+0.31}_{-0.63}$	–	25.40 ± 0.01
XID57	NL	10.49 ± 0.11	<45.10	<34	44.26 ± 0.18	58.9 ± 7.7	[b]$23.30^{+0.32}_{-0.39}$	$44.04^{+0.17}_{-0.24}$	–	<24.20
XID419	NL	10.89 ± 0.02	45.20 ± 0.04	42 ± 4	45.54 ± 0.05	70.2 ± 8.4	[b]$24.28^{+0.19}_{-0.31}$	$43.84^{+0.29}_{-0.44}$	–	<24.12
XID427	NL	10.87 ± 0.08	<45.43	<72	44.60 ± 0.13	324.2 ± 18.0	$22.43^{+0.24}_{-0.34}$	$43.20^{+0.06}_{-0.06}$	–	<24.20
XID522	NL	10.42 ± 0.02	46.26 ± 0.02	492 ± 25	45.02 ± 0.02	35.1 ± 5.9	[b]>22.5	$43.51^{+0.76}_{-0.87}$	–	24.37 ± 0.05
XID614	NL	10.78 ± 0.08	45.97 ± 0.02	247 ± 12	44.97 ± 0.13	78.3 ± 8.8	$24.25^{+0.19}_{-0.18}$	$43.61^{+0.18}_{-0.18}$	–	<24.26
cid_166	BL	10.38 ± 0.22	<45.92	<224	46.93 ± 0.02	717.8 ± 26.8	<21.25	$45.15^{+0.03}_{-0.02}$	9.3 ± 0.1 [c]	<24.00
lid_1289	NL	9.59 ± 0.14	<44.98	<25	45.09 ± 0.08	123.4 ± 11.1	$22.50^{+0.29}_{-0.22}$	$44.69^{+0.26}_{-0.13}$	–	<23.98
cid_1057	NL	10.84 ± 0.07	45.50 ± 0.02	85 ± 4	45.91 ± 0.06	36.1 ± 6.0	$23.98^{+0.24}_{-0.28}$	$44.53^{+0.26}_{-0.30}$	–	<23.89
cid_1605	BL	–	<45.54	<94	46.03 ± 0.02	327.9 ± 18.1	$21.77^{+0.51}_{-0.75}$	$44.69^{+0.06}_{-0.04}$	8.4 ± 0.2	<23.84
cid_337	NL	11.13 ± 0.04	45.63 ± 0.03	115 ± 9	45.34 ± 0.09	83.1 ± 9.1	<22.76	$44.22^{+0.11}_{-0.12}$	–	23.99 ± 0.07
cid_346[a]	BL	11.01 ± 0.22	46.13 ± 0.06	362 ± 49	46.66 ± 0.02	124.1 ± 11.1	$23.05^{+0.17}_{-0.19}$	$44.47^{+0.08}_{-0.09}$	8.9 ± 0.1 [c]	24.86 ± 0.07[d]
cid_451[a]	NL	11.21 ± 0.05	<45.67	<125	46.44 ± 0.07	136.9 ± 11.7	$23.87^{+0.19}_{-0.15}$	$45.18^{+0.23}_{-0.19}$	–	26.43 ± 0.01[d]
cid_1205	NL	11.20 ± 0.10	46.16 ± 0.04	384 ± 33	45.75 ± 0.17	33.9 ± 5.8	$23.50^{+0.27}_{-0.27}$	$44.25^{+0.21}_{-0.23}$	–	24.10 ± 0.06
cid_2682	NL	11.03 ± 0.04	<45.54	<93	45.48 ± 0.10	35.5 ± 6.0	$23.92^{+1.01}_{-0.20}$	$44.30^{+0.96}_{-0.27}$	–	<23.99
cid_1143[a]	NL	10.40 ± 0.17	45.61 ± 0.07	108 ± 18	44.85 ± 0.12	51.3 ± 7.2	$24.01^{+0.77}_{-0.29}$	$44.83^{+0.43}_{-0.36}$	–	24.39 ± 0.05
cid_467	BL	10.10 ± 0.29	<45.74	<147	46.53 ± 0.04	446.8 ± 21.1	$22.31^{+0.23}_{-0.32}$	$44.87^{+0.04}_{-0.05}$	8.9 ± 0.6	<23.92
cid_852	NL	11.17 ± 0.02	<45.57	<100	45.50 ± 0.11	25.0 ± 5.0	$24.30^{+0.38}_{-0.37}$	$45.20^{+1.14}_{-0.76}$	–	<23.90
cid_971	NL	10.60 ± 0.12	–	<96[e]	44.71 ± 0.24	33.1 ± 5.8	<23.68	$43.87^{+0.36}_{-0.38}$	–	<24.01

Notes. (1) Target ID, see also Table A.1; (2) AGN classification into broad line (BL) and narrow line (NL) according to the optical spectra; (3) Galaxy stellar mass and 1σ error; (4) FIR luminosity in the 8−1000 μm range and 1σ error; (5) SFR from the FIR luminosity and 1σ error; (6) AGN bolometric luminosity and 1σ error, derived from SED fitting; (7) X-ray net counts (i.e., background subtracted) in the full band and respective error, computed assuming a Poisson statistic; (8) Absorbing hydrogen column density and 90% confidence level error; (9) Absorption-corrected X-ray luminosity in the hard band (2−10 keV) and 90% confidence level error; (10) Black hole mass and 1σ error. For the XMM-XXL and Stripe82X targets the values are from Shen et al. (2015), for the WISSH targets are from Weedman et al. (2012), and for COSMOS we have re-analyzed zCOSMOS and FMOS spectra (Schulze et al., in prep.); (11) Radio power at 1.4 GHz and 1σ error. [(a)]Targets classified as "jetted" (Padovani 2017), according to the comparison between their IR and radio properties (see Fig. 7). [(b)]Targets fit with the physical model MYtorus (Murphy & Yaqoob 2009) that self-consistently takes into account photoelectric absorption, Compton scattering, cold reflection and fluorescent emission in a fixed toroidal geometry. The analysis was performed as described in Lanzuisi et al. (2018). [(c)]BH mass derived using the Hβ emission line from Subaru/FMOS spectroscopy (Schulze et al., in prep.). [(d)]Targets detected at 1.4 GHz as part of the VLA-COSMOS survey (Schinnerer et al. 2007). The luminosities reported here for these targets are derived from the 1.4 GHz fluxes. The predicted 3 GHz fluxes (assuming $\alpha_{\rm r} = 0.7$) are consistent with the observed 1.4 GHz ones for cid_1253 and cid_346, while for cid_451 the predicted flux is a factor of 2 higher than the measured 1.4 GHz one. The measurements reported for the other COSMOS targets are derived from 3 GHz fluxes (see Sect. 4.3). [(e)]Average SFR over the last 100 Myr of the galaxy history as obtained from the modeling of the stellar component with SED fitting. [(f)]BH mass derived using the Hβ emission line from Bischetti et al. (2017).

Table A.2. continued

ID	AGN type	$\log \frac{M_*}{M_\odot}$	$\log \frac{L_{\rm FIR}}{\rm erg\,s^{-1}}$	SFR ($M_\odot\,{\rm yr}^{-1}$)	$\log \frac{L_{\rm bol}}{\rm erg\,s^{-1}}$	X-ray net counts	$\log \frac{N_{\rm H}}{\rm cm^{-2}}$	$\log \frac{L_{[2-10\,{\rm keV}]}}{\rm erg\,s^{-1}}$	$\log \frac{M_{\rm BH}}{M_\odot}$	$\log \frac{P_{1.4\,{\rm GHz}}}{\rm W\,Hz^{-1}}$
(1)	(2)	(3)	(4)	(5)	(6)	(7)	(8)	(9)	(10)	(11)
cid_38	NL	11.01 ± 0.12	<45.98	<258	45.78 ± 0.04	159.4 ± 12.6	<22.95	$44.41^{+0.16}_{-0.13}$	–	24.10 ± 0.05
lid_206	BL	10.30 ± 0.25	–	63 ± 27^{e}	44.77 ± 0.12	40.2 ± 6.3	<22.55	$43.91^{+0.39}_{-0.29}$	7.9 ± 0.1	<23.94
cid_1253	NL	10.99 ± 0.25	46.02 ± 0.30	280 ± 194	45.08 ± 0.18	36.1 ± 6.0	$23.22^{+0.47}_{-0.39}$	$43.92^{+0.29}_{-0.31}$	–	24.30 ± 0.08^{d}
J1333+1649[a]	BL	–	–	–	47.91 ± 0.02	174.5 ± 13.2	$21.81^{+0.22}_{-0.34}$	$45.81^{+0.07}_{-0.06}$	9.79 ± 0.3	28.15 ± 0.01
J1441+0454	BL	–	–	–	47.55 ± 0.02	74.5 ± 8.6	$22.77^{+0.18}_{-0.21}$	$44.77^{+0.10}_{-0.11}$	10.2 ± 0.3	25.78 ± 0.03
J1549+1245	BL	–	–	–	47.73 ± 0.04	1023.1 ± 32.0	$22.69^{+0.09}_{-0.11}$	$45.38^{+0.02}_{-0.02}$	10.1 ± 0.3^{f}	25.91 ± 0.03
S82X1905	BL	–	–	–	46.50 ± 0.02	31.3 ± 5.6	$22.95^{+0.35}_{-0.17}$	$44.91^{+0.50}_{-0.50}$	9.3 ± 0.1	<24.79
S82X1940	BL	–	–	–	46.03 ± 0.02	33.7 ± 5.8	<20.50	$44.72^{+0.30}_{-0.30}$	8.7 ± 0.2	<24.83
S82X2058	BL	–	–	–	46.39 ± 0.02	29.5 ± 4.3	<20.50	$44.67^{+0.30}_{-0.30}$	8.9 ± 0.3	<24.81
S82X2106	BL	–	–	–	46.08 ± 0.03	94.5 ± 9.7	<22.08	$45.08^{+0.08}_{-0.11}$	9.2 ± 0.1	<24.80

Appendix B: Description of the photometric catalog

Table B.1. Column description of the photometric catalog.

Column number	Label	Description
1	ID	ID of each target as given in Table A.1
2	z	Redshift
3, 4	NUV_galex, NUV_galex_err	GALEX NUV flux and error
5, 6	U_ctio, U_ctio_err	CTIO-Blanco/Mosaic-II U-band flux and error
7, 8	U_vimos, U_vimos_err	VLT/VIMOS U-band flux and error
9, 10	u_megacam, u_megacam_err	CFHT/MegaCam u-band flux and error
11–20	u_sloan, ..., z_sloan_err	SDSS fluxes and errors
21–30	B_subaru, ..., z_subaru_err	Subaru/Suprime-Cam fluxes and errors
31–42	WFI_U, ..., WFI_I_err	ESO-MPG/WFI fluxes and errors
43–52	acs_f435w, ..., acs_f850lp_err	HST/ACS fluxes and errors
53–60	wfc3_098M, ..., wfc3_H160W_err	HST/WFC3 fluxes and errors
61–72	u_cfhtl, ..., z_cfhtl_err	CFHT fluxes and errors
73–76	J_ctio, ..., Ks_ctio_err	CTIO-Blanco/ISPI fluxes and errors
77, 78	z_ctio, z_ctio_err	CTIO-Blanco/Mosaic-II z-band flux and error
79–88	VISTA_Z, ..., VISTA_Ks_err	VISTA fluxes and errors
89–94	J_ukidss, ..., K_ukidss_err	UKIDSS fluxes and errors
95, 96	H_sofi, H_sofi_err	NTT/SofI H-band flux and error
97, 98	isaac_Ks, isaac_Ks_err	VLT/ISAAC K_s-band flux and error
99, 100	HAWKI_Ks, HAWKI_Ks_err	VLT/HAWK-I K_s-band flux and error
101–108	Y_uv, ..., K_uv_err	VISTA/VIRCAM fluxes and errors
109, 110	Y_hsc, Y_hsc_err	Subaru/HSC Y-band flux and error
111–114	H_w, ..., K_w_err	CFHT/WIRCam fluxes and errors
115–120	J_2mass, ..., Ks_2mass_err	2MASS fluxes and errors
121–128	irac_ch1, ..., irac_ch4_err	*Spitzer*/IRAC fluxes and errors
129–136	W1, ..., W4_err	WISE fluxes and errors
137–138	mips24, mips24_err	*Spitzer*/MIPS 24 μm flux and error
139–144	pacs70, ..., pacs160_err	*Herschel*/PACS fluxes and errors
145–150	spire250, ..., spire500_err	*Herschel*/SPIRE fluxes and errors
151–154	ALMA_band7, ..., ALMA_band3_err	ALMA Band 7 and 3 fluxes and errors

Notes. The catalog is available at the CDS.

Appendix C: Spectral energy distributions of the SUPER sample

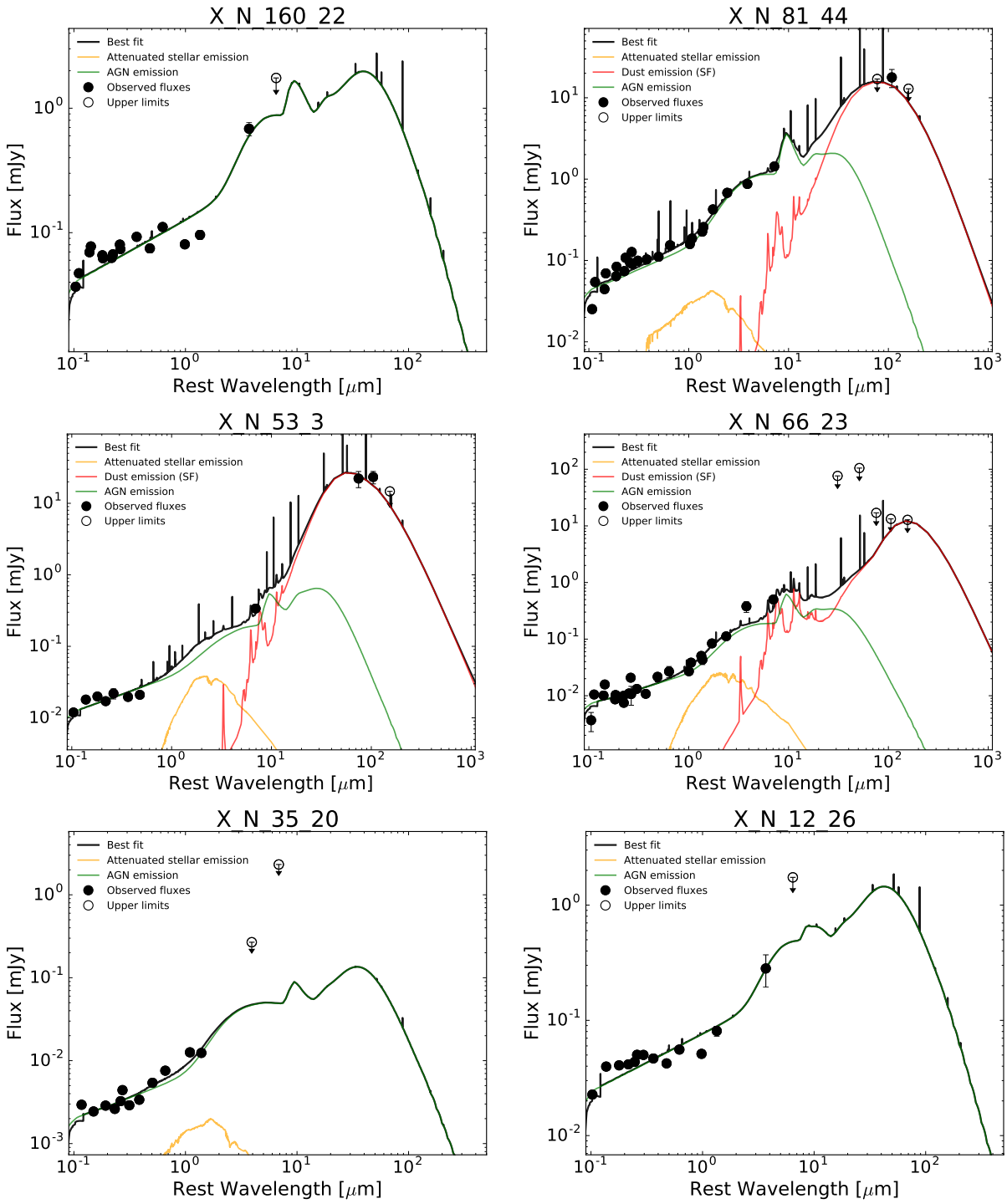

Fig. C.1. Rest-frame SEDs of the whole SUPER sample. The black dots represent the observed multi-wavelength photometry, while the empty dots indicate 3σ upper limits. The black solid line is the total best-fit model, the orange curve represents the stellar emission attenuated by dust, the green template reproduces the AGN emission, the red curve accounts for dust emission heated by star formation. Emission lines in the black curves are part of the nebular emission component, included in the overall SED.

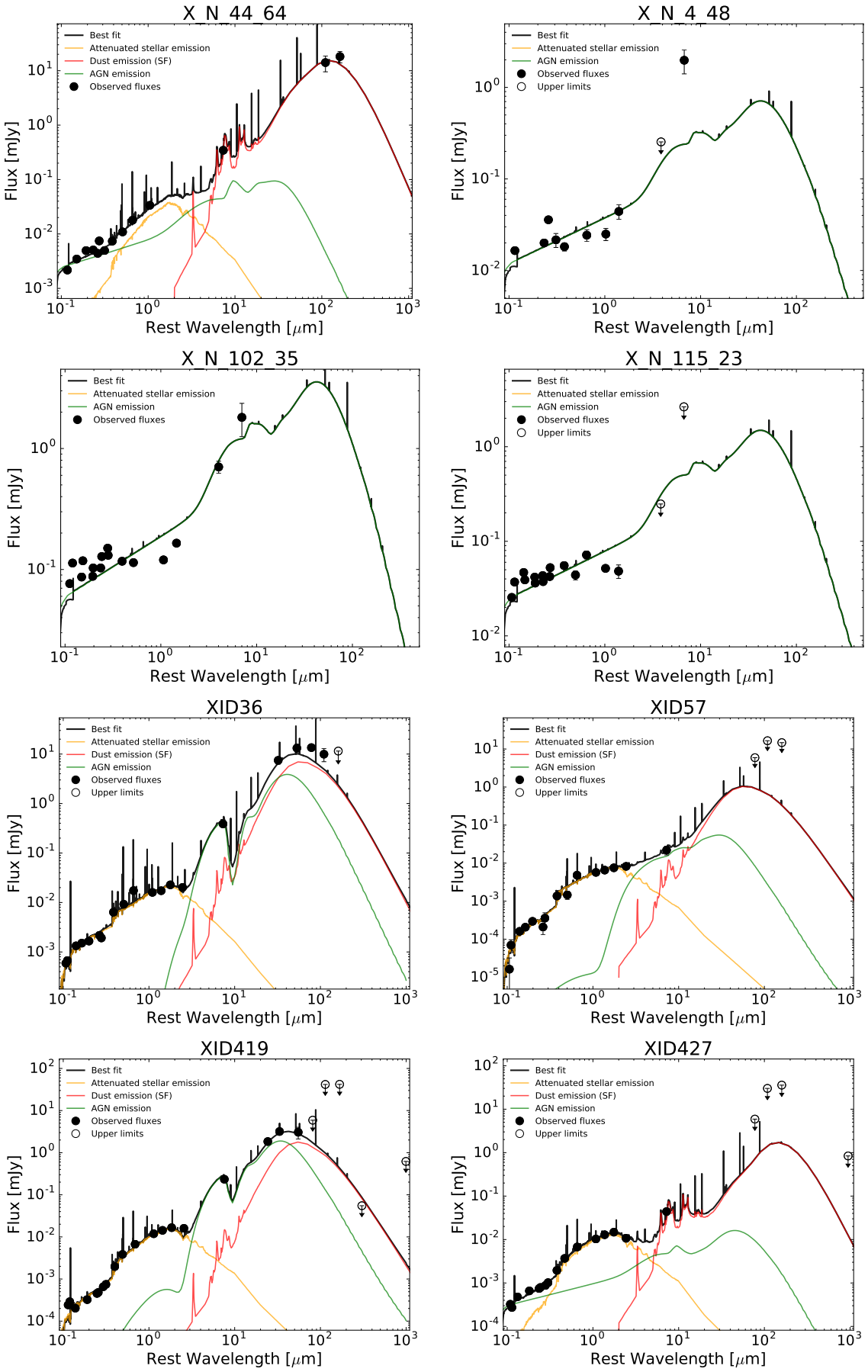

Fig. C.1. continued.

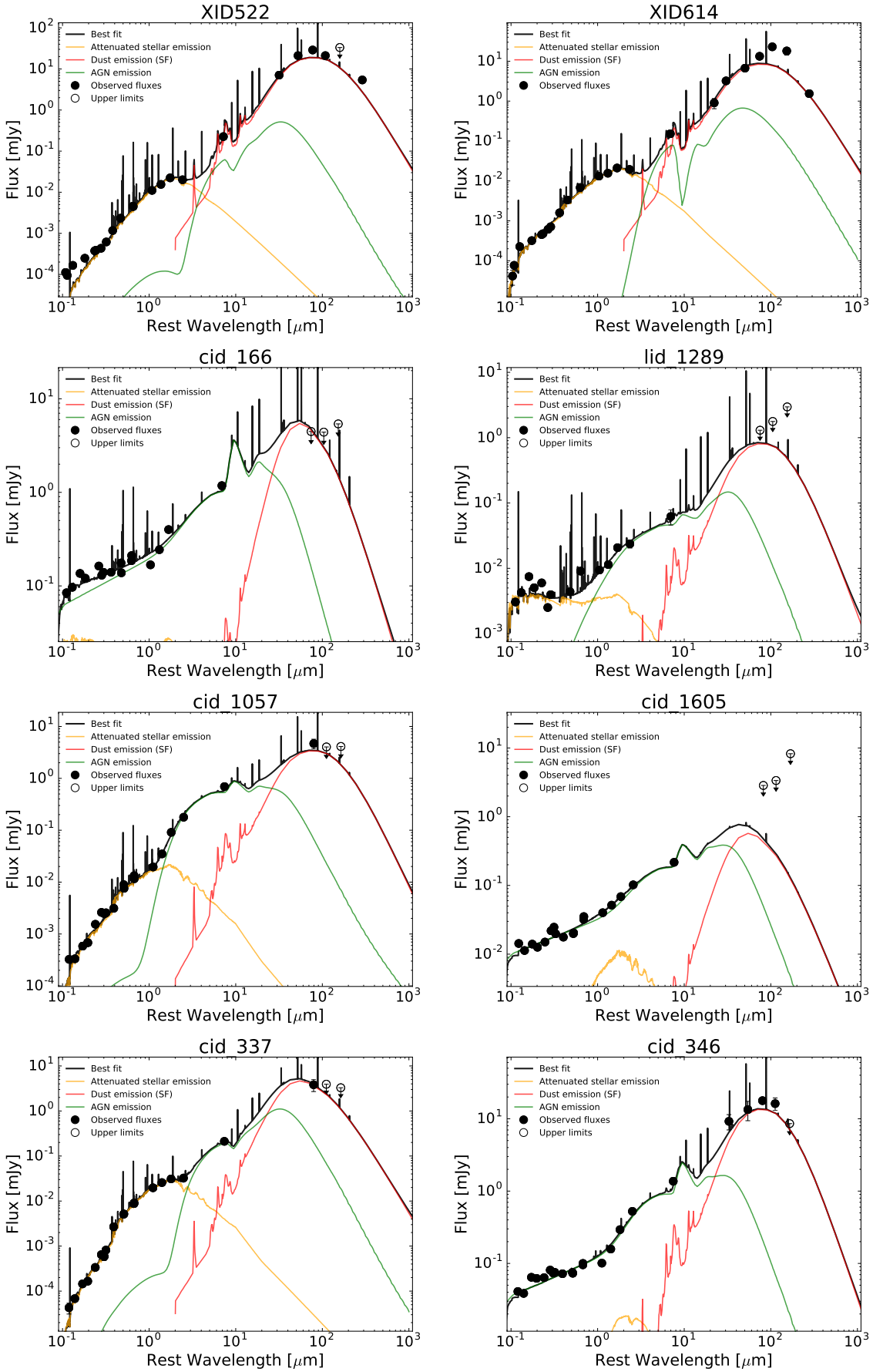

Fig. C.1. continued.

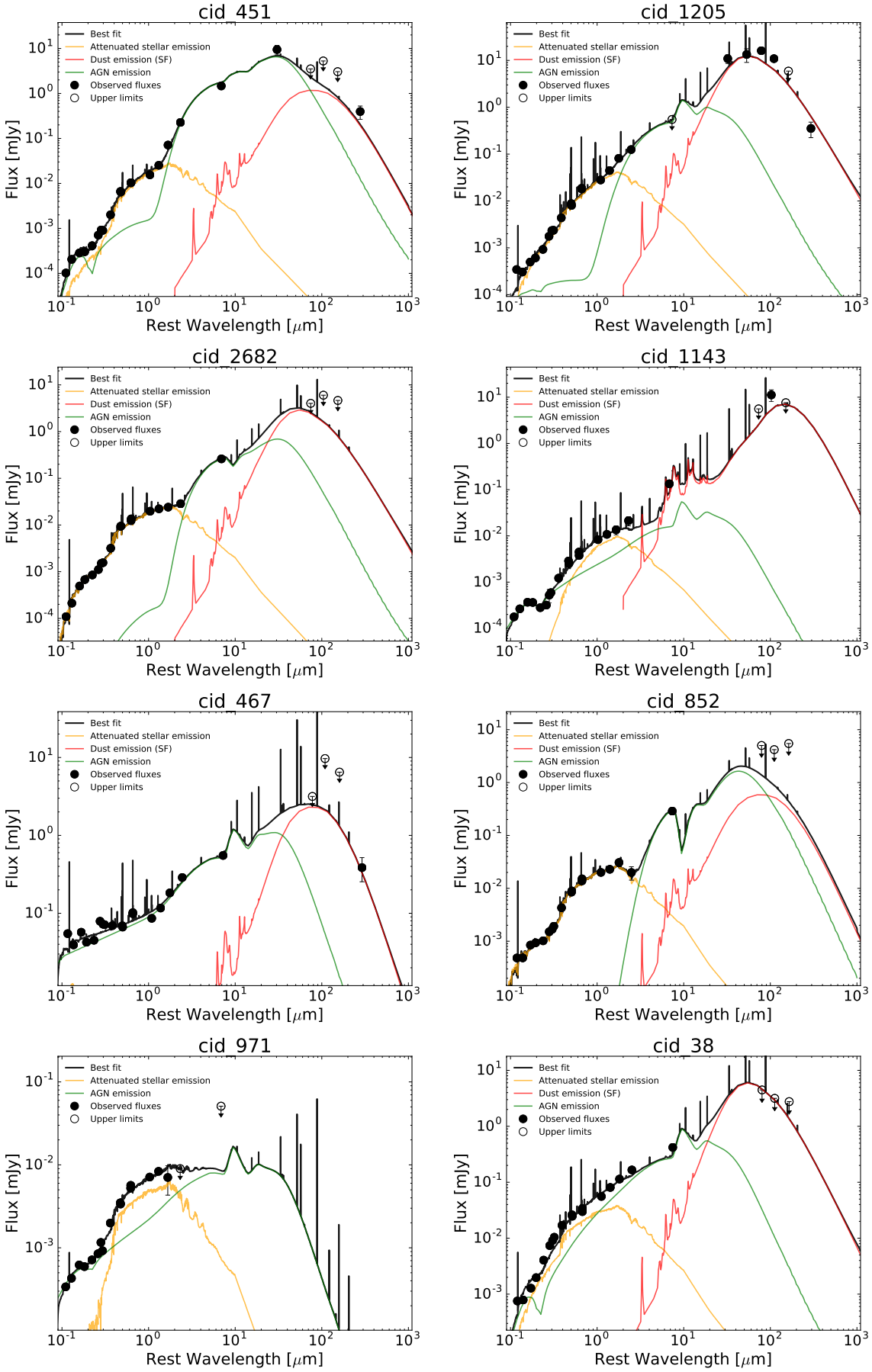

Fig. C.1. continued.

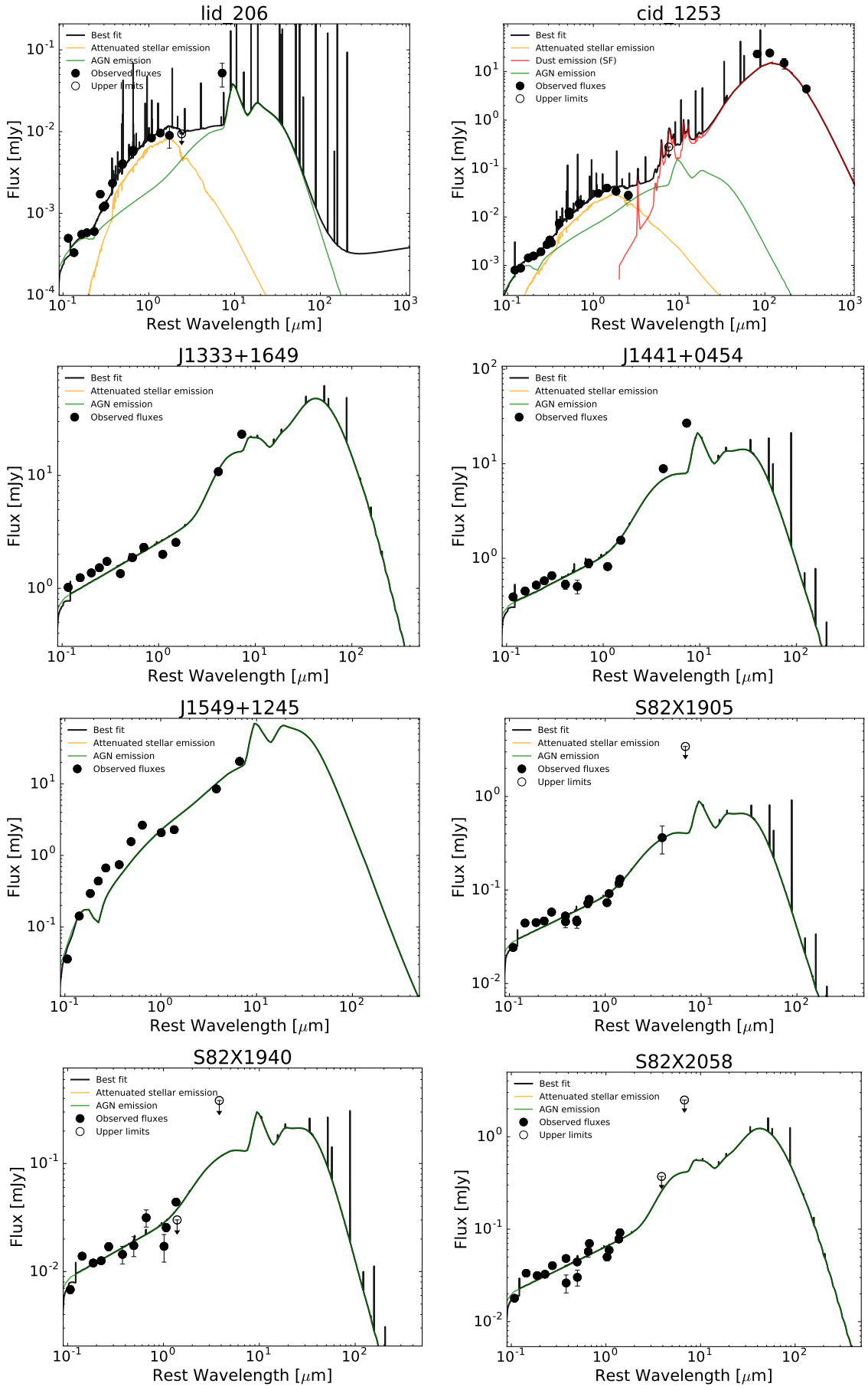

Fig. C.1. continued.

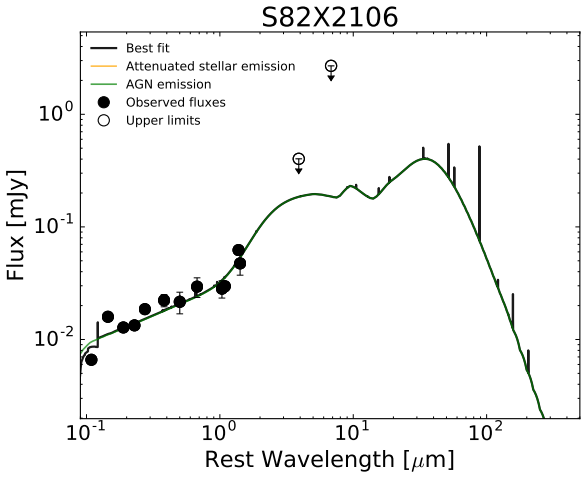

Fig. C.1. continued.